Civil and Environmental Engineering Master's Project Reports

Civil and Environmental Engineering

Spring 2023

Liquefaction Triggering in Low-Plasticity Silts and Effects of Liquefaction-Induced Lateral Spreading on a Reinforced-Concrete Pile

Jared A. Martinez
Portland State University

Recommended Citation

Martinez, Jared A., "Liquefaction Triggering in Low-Plasticity Silts and Effects of Liquefaction-Induced Lateral Spreading on a Reinforced-Concrete Pile" (2023). *Civil and Environmental Engineering Master's Project Reports*. 62.
https://doi.org/10.15760/CCEMP.61

LIQUEFACTION TRIGGERING IN LOW-PLASTICITY SILTS AND EFFECTS OF LIQUEFACTION-INDUCED LATERAL SPREADING ON A REINFORCED-CONCRETE PILE

BY

JARED A. MARTINEZ

A research project report submitted in partial fulfillment
of the requirement for the degree of

MASTER OF SCIENCE
IN
CIVIL AND ENVIRONMENTAL ENGINEERING

Project Advisor:
Dr. Arash Khosravifar

Portland State University

ACKNOWLEDGMENTS

The test data presented in Chapter 2 (Undrained Cyclic Shear Behavior of A Low Plasticity Alluvial Silt) were performed at Portland State University for Shannon & Wilson in support of a transportation project in Portland, Ore. We are thankful to Shannon & Wilson for releasing the data to be presented in this study and the corresponding publication (Martinez et al. 2023). Graduate students, Kayla Sorenson and Stephanie Meister, helped with laboratory tests at Portland State University. For further information, see the Martinez et al. 2023 reference.

The shake table test data used in Chapter 3 (Combined Effects of Liquefaction-Induced Lateral Spreading and Superstructure Inertial Loads on Pile Foundations) were provided by Professor Ahmed Elgamal and Dr. Ahmed Ebeido of University of California at San Diego (UCSD). Chapter 3 of this report explains recent analysis performed at PSU and presented in Martinez et al. (2022). Support for the analyses at PSU was provided by Grant No. CPF-2020-DRSH-2 from the Deep Foundations Institute and Portland State University. The support for the shake table test conducted at UCSD was provided by the California Department of Transportation with Dr. Charles Sikorsky as the Program Manager. Soil pressure and Pore Pressure transducers used in liquefaction testing were provided by Kyowa Americas Inc. and their technical support is gratefully appreciated. Any opinions, findings, and conclusions or recommendations expressed in this article are those of the author(s) and do not necessarily reflect the views of the funding agencies.

Thank you to my fellow graduate students, my professors Dr. Khosravifar and Dr. Moug, and thank you to my wife for the support given during my studies.

ABSTRACT

Liquefaction triggering and post-liquefaction effects on lateral loading of deep foundations is an emerging area of study. This project presents: the results of cyclic direct simple shear (CDSS) testing on a low-plasticity alluvial silt collected in Portland, Oregon; and analysis of the combined effects of liquefaction-induced lateral spreading on a reinforced-concrete pile using data collected from a shake table test. The former research determines the liquefaction susceptibility and post-liquefaction characteristics of a local transitional soil using stress-controlled CDSS testing, the latter explores the complex lateral loading a reinforced-concrete pile undergoes during seismic loading with liquefaction-induced lateral spreading of the ground surface. This project presents the research performed to comment on liquefaction susceptibility and its effects on deep foundations.

TABLE OF CONTENTS

LIST OF TABLES

LIST OF FIGURES

1.0 INTRODUCTION

Current geotechnical seismic design practices largely consider the cyclic behavior of fine-grained soils as either sand-like or clay-like. The methods for classifying soils as either sand-like or clay-like come from empirically-based relationships (Simpson and Evans 2016, Dahl et al. 2014, Sanin and Wijewickreme 2011, Vucetic and Dobry 1991). However, cyclic behavior of transitional soils, including non-plastic and low-plasticity silty sands and sandy silts are generally poorly defined. Commonly used screening methods suggest that the behavior of fine-grained soils transitions from liquefaction (sand-like behavior) to cyclic softening (clay-like behavior) at Plasticity Index (PI) ranging between 3 and 7 (Idriss and Boulanger 2008) and liquefiable to non-liquefiable at PI ranging between 12 and 18 (Bray and Sancio 2006). While these screening methods are often used as a preliminary measure, the high fines content and plasticity of these soils sometimes allow for collecting intact samples with little disturbance for laboratory testing and evaluation of the cyclic shear resistance of these transitional soils.

Transitional soils in the Pacific Northwest region of North America are often encountered in alluvial deposits along active, low grade rivers. These attributes indicate that they are likely susceptible to liquefaction based on their geologic age and deposition type (Youd and Perkins 1978). Consequently, in the Pacific Northwest, these soils must frequently be evaluated for liquefaction susceptibility in seismic vulnerability studies of infrastructure projects.

The study presented in section 2 examines laboratory test results on transitional soils from a major infrastructure project in Portland, Oregon (Martinez et al., 2023). Laboratory testing for this project included consolidation tests, cyclic direct simple shear (CDSS) and monotonic directs simple shear (MDSS). Tests were performed on intact samples from a Willamette River Silt deposit, with index properties that would indicate the soils are susceptible to liquefaction with the commonly used screening methods (Bray and Sancio 2006, Idriss and Boulanger 2008). The intact samples were collected using mud rotary drilling methods and Shelby tube sampling. The testing apparatus and laboratory testing protocols used follow manufacturer and ASTM standards.

Investigations of earthquakes in the recent past indicate that liquefaction-induced lateral spreading is a major cause of failure in pile-supported structures (e.g., Hamada et al. 1986, Turner et al. 2016, Cubrinovski et al. 2017). It is expected that pile foundations are designed to sustain the individual effects of lateral spreading and superstructure inertia. Currently, however, there is no consensus in the design codes and standards regarding whether these two loads should be combined when estimating pile demands. Some studies suggest that the two loads do indeed interact during earthquakes (e.g., Boulanger et al. 2007, Caltrans 2012); other studies recommend that for most earthquakes, the two loads can be treated as out-of-phase and uncoupled (e.g., MCEER/ATC 2003, Tokimatsu et al. 2005). Some design guidelines that are commonly used for highway bridges and wharf structures are listed in Table 1. The varying recommendations provided in this table highlight the site-and project-specific aspects of the interaction of inertial and kinematic loads due to liquefaction-induced lateral spreading.

Several shake table tests have been recently performed on pile foundations subjected to liquefaction-induced lateral spreading at research facilities in the US and Japan (e.g., Ebeido et al. 2019a, Ebeido et al. 2019b, Ebeido and Elgamal 2019a, and Ebeido and Elgamal 2019b). The study presented section 3 (Martinez et al, 2022) uses one of those shake table tests that was conducted at the University of California, San Diego (Ebeido 2019). This specific shake table experiment was performed on a reinforced concrete (RC) pile that was subjected to combined effects of liquefaction-induced lateral spreading and superstructural inertial. Section 3 briefly describes the experimental setup used in the study, followed by the presentation of representative inertial and kinematic loads. The load transfer mechanism within the non-liquefiable crust is characterized based on normal (perpendicular) soil pressures that were recorded using pressure transducer arrays mounted on the upside and downslide faces of the pile. The critical cycles are determined based on the response of the pile during shaking, and the magnitudes of inertial and kinematic loads and their interaction factors are calculated for each critical cycle. The implications of these findings for the design of pile foundations on sloping liquefiable soils are also presented.

Table 1. Current design guidelines for combining inertial and kinematic demands on piles

Design Code	Recommendation
AASHTO (2020)	Piles should be designed for independent (de-coupled) effects of inertial and lateral spreading loads; the two loads should be combined only for large magnitude earthquakes (M>8).
MCEER/ATC (2003)	For most earthquakes, peak inertia is likely to occur early in the ground motion; therefore, piles should be designed for independent (de-coupled) effects of inertial and lateral spreading loads. The two loads may interact for large magnitude and long-duration earthquakes.
PEER (2011) (Ashford et al. 2011)	100% kinematic + (65% to 85%) inertial (multiplied by 0.35 to 1.4 to account for the effects of liquefaction on peak inertial load)
Caltrans (2012) and ODOT (2014)	100% kinematic + 50% inertial
WSDOT (2021)	100% kinematic + 25% inertial when earthquakes with M>7.5 contribute to more than 20% of the hazard for peak ground acceleration
ASCE 61-14 (2014) Section C4.7 and Port of Long Beach Wharf Design Criteria (POLB 2015)	Locations of maximum bending moments from inertial and lateral ground deformation are spaced far enough apart that the two loads do not need to be superimposed. Maximum bending moments occur at different times. The two loads should be treated as uncoupled for marginal wharves.
Port of Anchorage Modernization Program Seismic Design Manual (POA 2017)	Combine peak inertial loading from earthquake ground motion with 100% peak kinematic demands from lateral ground displacements. Smaller factors are allowed if peer-reviewed two-dimensional nonlinear numerical analysis is used (no less than 25%).

2.0 UNDRAINED CYCLIC SHEAR BEHAVIOR OF A LOW PLASTICITY ALLUVIAL SILT

2.1 Laboratory Testing Program

A laboratory testing program was performed to characterize the cyclic behavior of the soils in respect to their susceptibility to liquefaction and cyclic softening. The testing included 7 stress-controlled CDSS tests with post-cyclic testing (either recompression or monotonic shear), 2 static MDSS tests, 3 consolidation tests, and index tests including grain size distribution analysis and Atterberg limits.

CDSS and MDSS tests were performed using a constant-volume apparatus with an active control system where pore pressures are determined based on changes in vertical stress (ASTM D8296). The vertical strains during cyclic loading in this study were generally lower than 0.02% which is within the 0.05% maximum threshold allowed by ASTM standards for monotonic DSS under constant volume conditions (except for Cyclic01 where vertical strains reached 0.1% during cyclic loading). The samples were incrementally consolidated to a maximum vertical stress and then unloaded to a lower stress prior to cyclic or monotonic shear tests to mechanically create overconsolidation ratios of 1.5 and 1.875. Cyclic shear stresses were applied at a frequency of 0.1 Hz, cyclic loading was performed until approximately 10% double amplitude shear strain was achieved, or a maximum cycle count of 200 was reached. A post-cyclic test followed, consisting of either reconsolidation of the specimen to the pre-cyclic vertical stress, or a post-cyclic monotonic shear at constant volume. All cyclic tests performed herein were stress-controlled with uniform loading to a specified CSR (equal to the shear stress divided by the pre-cyclic vertical consolidation stress). Cyclic failure was considered when single amplitude (SA) shear strain reached 3%.

MDSS tests (static and post-cyclic) were performed at a rate of 0.05 inches per hour, which corresponds to an approximate shear strain rate of 5% per hour and were performed to a maximum displacement of 0.2 inches (20% shear strain). Consolidation tests were performed using incremental stress methods following ASTM D2435. Atterberg limits were determined using the ASTM D4318 methods. Sand and fines content were determined following the sieve and wash procedures in ASTM D6913. Silt and clay content were determined following the hydrometer analysis procedures in ASTM D7928.

Table 2 presents a summary of the CDSS, MDSS, and consolidation testing parameters and basic specimen properties. The pre-test water contents were measured from trimmings during sample preparation and the pre-test total densities were measured on the specimen (1-inch height and 2.5-inch diameter) prior to placement in the device. The pre-test calculated void ratio ranged between 0.82 and 1.08 based on an assumed specific gravity of Gs=2.7. Table 3 lists specimen index properties. The presented silt fractions indicate particles with sizes between 0.075 and 0.002 mm, and the presented clay fractions indicate particles with sizes less than 0.002 mm.

Table 2: Testing parameters for CDSS, MDSS and consolidation tests.

Boring and Sample ID	Specimen	Avg. Depth (ft)	Pre-Test Water Content (%)	Pre-test Total Wet Density (kg/m^3)	Max. Consol. Vert. Stress (kPa)	Vert. Stress Prior to Shear (kPa)	CSR (at 0.1 Hz Loading)	Total Number of Cycles
B32 U1	Cyclic01	53.5	33.7	1839	300	200	0.22	13
B32 U1	Cyclic03	54.2	35.6	1849	300	200	0.175	200*
B32 U1	Cyclic04	54.2	41.6	1799	300	200	0.200	19
B15 U2	Cyclic05	59.0	39.4	1784	330	220	0.191	28
B15 U2	Cyclic06	59.2	41.7	1758	330	220	0.177	29
B15 U2	Cyclic07	59.5	41.1	1781	330	220	0.155	200*
B4 U1	Cyclic08	30.6	43.8	1798	300	160	0.225	14
B32 U1	Mono01	54.8	39.8	1804	300	200	---	---
B15 U2	Mono02	59.8	37.7	1764	330	220	---	---
B32 U1	Consol01	53.1	32.5	1830	1600	---	---	---
B15 U2	Consol02	58.7	38.0	1778	3200	---	---	---
B4 U1	Consol04	30.2	35.2	1835	3200	---	---	---

*These specimens reached the maximum number of designated cycles

Table 3: Index properties of test specimens

Boring and sample ID	Specimen	Atterberg Limits			Wash Data	Hydrometer data	
		LL	PL	PI	% Fines	%Silt	%Clay
B32 U1	Cyclic01	36	33	3	48.1		
B32 U1	Cyclic03	41	36	5	59.7		
B32 U1	Cyclic04	39	34	5	45.9		
B15 U2	Cyclic05	38	37	1	49.9		
B15 U2	Cyclic06	38	38	NP	44.5		
B15 U2	Cyclic07	38	38	NP	54.1		
B4 U1	Cyclic08	29	30	NP	71.1	65.4	5.7
B32 U1	Mono01	38	34	4	39.6	32.1	7.5
B15 U2	Mono02	37	35	2	36.5		
B32 U1	Consol01	35	31	4	53.4		
B15 U2	Consol02	37	38	NP	54.0	45.4	8.6
B4 U1	Consol04	30	25	5	67.7		

NP: Nonplastic

2.2 Sample quality assessment

Sample quality was determined by analyzing the 1D consolidation tests using the following approaches: Specimen Quality Designation (SQD) (Terzaghi et al. 1996), void ratio based (Lunne et al. 1997), and the work-based framework for low plasticity soils (DeJong et al. 2018). The results for each approach are presented in Table 4. The Lunne et al. and SQD methods were developed with soils containing greater fines and PI than specimens in this study. DeJong et al. (2018) notes that sample quality is generally over-estimated in low plasticity soils by the Lunne et al. and SQD methods, however in our samples we see relatively poorer ratings using these frameworks when compared to work-based designation. This may be due to the specific soil and confining stresses used in this testing series. The combined assessment from the three methods suggests that the specimens may have been subjected to sample disturbance which is consistent with sample qualities seen in testing series on similar materials.

Table 4: Sample quality summary

Sample	Specimen	SQD	$\Delta e/e_0$	Lunne et al. Descriptor	Work-based designation
B32U1	Consol01	D	0.10	Poor	High
B15U2	Consol02	D	0.045	Good to fair	High
B4U1	Consol04	D	0.095	Poor	High

2.3 Test Results

Stress History and Over-consolidation Ratio.

Figure 1 shows the 1D consolidation test results for three specimens, one from each Shelby tube used for cyclic testing. Using Casagrande method (Casagrande 1936; ASTM D2435), the preconsolidation stress for B32U1 (using Consol01) was estimated between 250 and 400 kPa (best estimate 300 kPa), the preconsolidation stress for B15U2 (using Consol02) was estimated between 410 and 510 (best estimate 490 kPa), and the preconsolidation stress for B4U1 (using Consol04) was estimated between 310 and 540 kPa (best estimate 480 kPa).

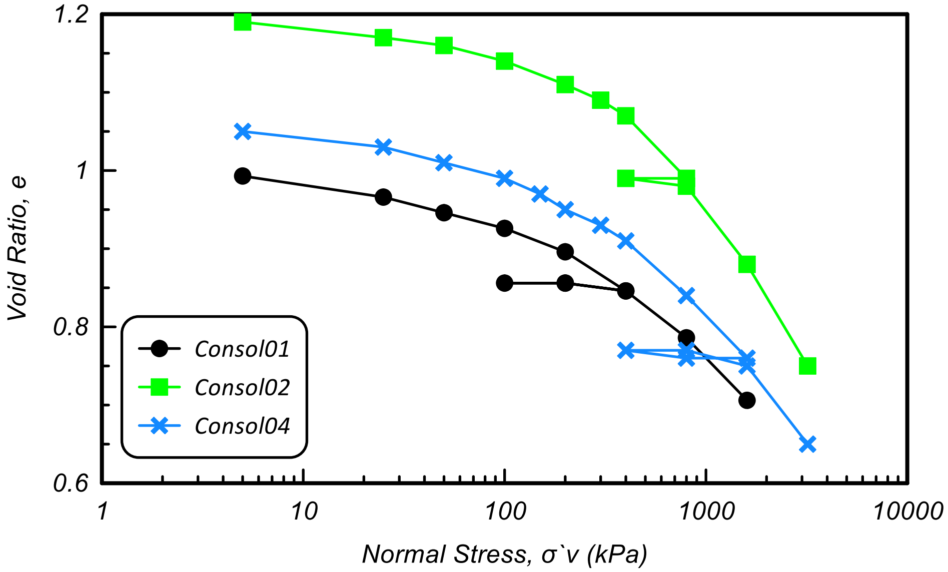

Figure 1: 1D Consolidation testing summary

The dissipated Strain Energy (DSE) method developed by Wang and Frost (2004) was also performed using the consolidation samples to estimate preconsolidation stresses of 381 kPa for B32U1 (Consol01), 485 kPa for B15U2 (Consol02), and 583 kPa (for Consol04).

For the purposes of this report, over-consolidation ratios (OCR) of the soil specimens will be presented as OCR_{lab} based on the mechanically consolidated values performed on the specimens within the testing apparatus (Table 2). The OCR_{lab} value is being used due to the relative disturbance of the soils introducing uncertainty in estimating the likely preconsolidation stress for the soil. This is a common concern with low-plasticity intact samples (Lunne et al. 1997).

The OCR_{lab} values of 1.5 and 1.875 correspond to expected OCR of in-situ conditions based on correlations of Standard Penetration Testing (SPT), Cone Penetration Testing (CPT), and select constant strain consolidation tests performed for the project's site characterization. The maximum consolidation vertical stresses applied on the lab specimens were approximately 10 percent greater than the interpreted preconsolidation stresses in-situ.

Undrained Monotonic Shear Strength.

Monotonic shear tests were performed on specimens collected from two of the intact samples with the properties noted in Table 2. These results are shown in Figure 2 and show slightly contractive behavior as indicated by reduced vertical effective stress during shear. The static undrained shear strength, referenced herein as S_u, for each static MDSS test was extracted at a reference shear strain of 10% and will be used to normalize cyclic and post-cyclic responses presented later.

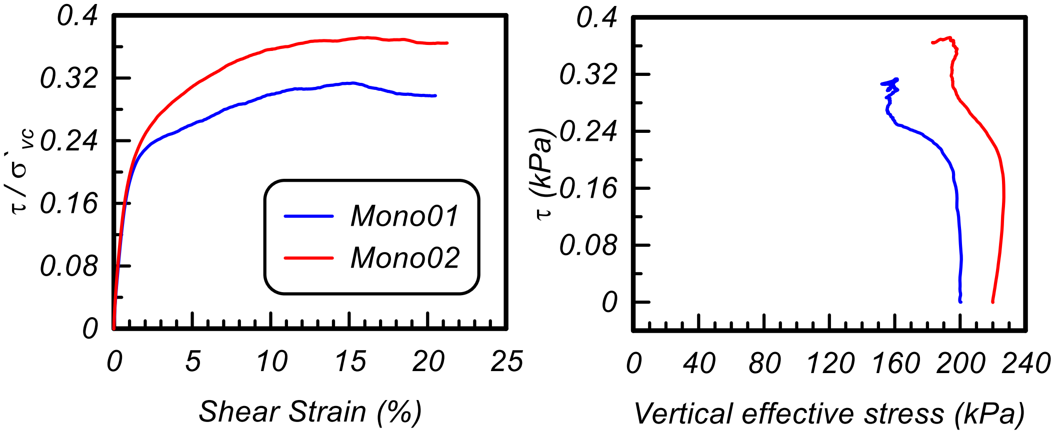

Figure 2: Monotonic DSS Results (a) Shear stress vs. shear strain (b) Shear stress vs vertical effective stress

Undrained Cyclic Shear Strength.

Figure 3 graphically presents the cyclic testing results. Table 5 presents a summary of cyclic and post-cyclic testing results. Figures 3a displays the CSR – shear strain hysteretic loops. Figures 3b show the measured shear strain against the total cycle count, *N*. Figures. 3c show the excess porewater pressure ratio, r_u, defined as the excess pore water pressure divided by the pre-cyclic vertical consolidation stress ($\sigma`_{vc}$), against *N*. Figure 3d reports the CSR against the normalized vertical stress ($\sigma`_v/\sigma`_{vc}$), commonly referred to as the effective stress path of the specimen during cyclic testing

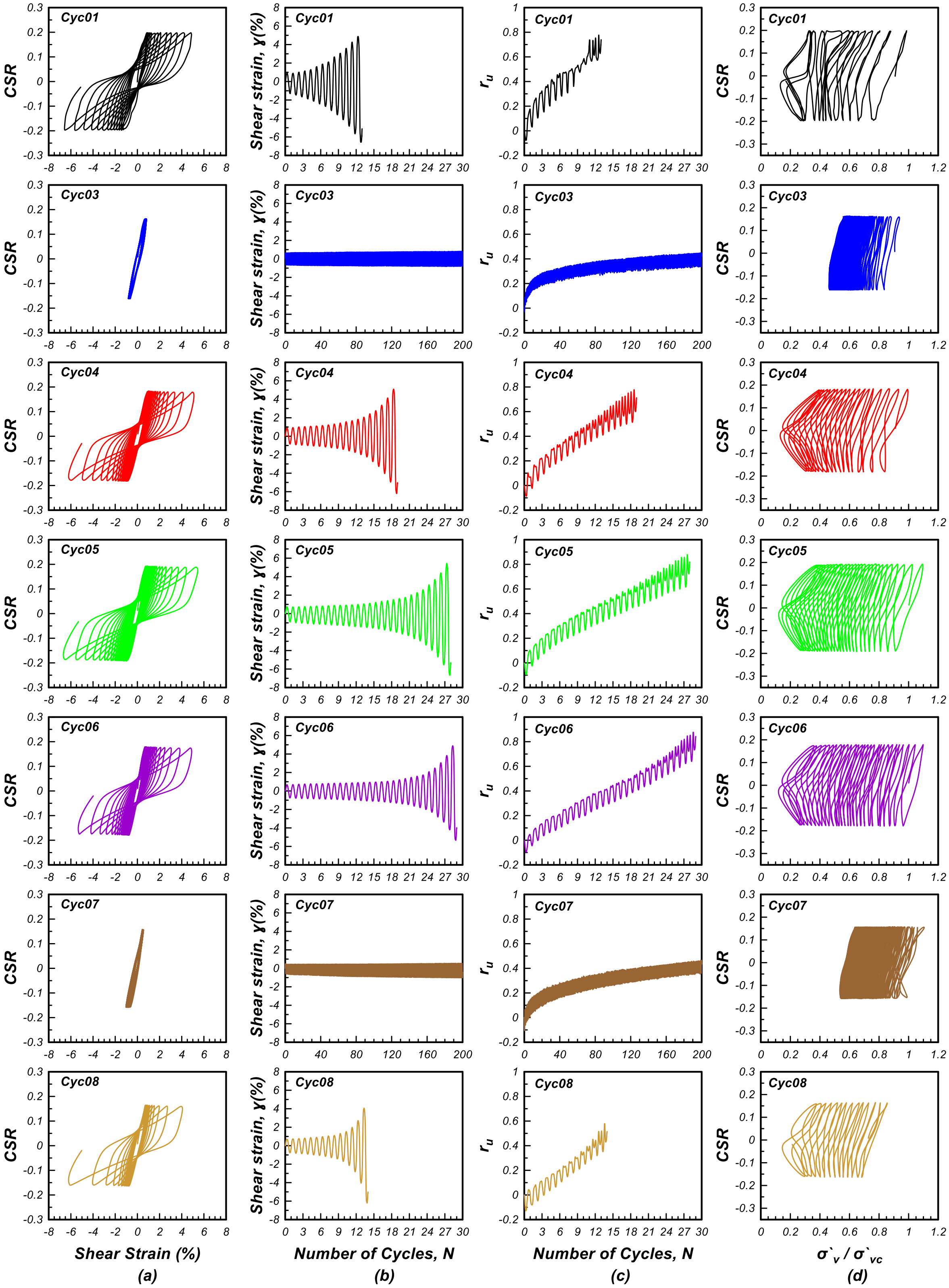

Figure 3: (a) shear stress- shear strain hysteresis, (b) shear strain, (c) excess pore pressure, and (d) effective stress path development during cyclic loading

Figure 4a shows the variation of CSR with number of loading cycles to reach 3% SA shear strain. The cyclic shear stress values presented here are adjusted to equivalent 1 Hz loading by increasing the applied shear stress by 9% as used in other studies (e.g., Dahl et al. 2014). A power equation was fit using $CSR = a*N^{-b}$. The exponent parameter (b) was found to be 0.160 which is within the range reported by other studies for fine grained soils (Idriss and Boulanger 2008). Data by other studies on similar soils are plotted for comparison showing a general increase in CRR (CSR at 15 cycles) with OCR and plasticity.

Figure 4b shows the rate-adjusted shear stress normalized by undrained shear strength, S_u. S_u was measured from static MDSS tests at 10% shear strain for the specimens with OCR_{Lab} = 1.5. S_u was estimated for the specimen with OCR_{Lab} = 1.9 using the SHANSEP relation where $S_u/σ`_{vc} = S*OCR^{0.8}$ (Ladd and Foott, 1973), and the *S* parameter was estimated to be 0.237 by taking the average *S* calculated from the performed monotonic shear tests. Data by other studies is shown for comparison, showing a general agreement with the tests ran for this study and similar soils.

Table 5: Select cyclic and post-cyclic test results

Sample ID	CSR	No. of cycles to 3% SA shear strain	Max. shear strain during cyclic loading (%)	Maximum Ru during cyclic loading	Type of post-cyclic test	Post-cyclic *Su* (kPa) at γ=10%	Post-cyclic volumetric strain (%)
Cyc01	0.22	8	6.5	0.8	Shear	35	--
Cyc03	0.175	N/A	0.8	0.46	Reconsolidation	--	0.3
Cyc04	0.2	15	6.0	0.8	Reconsolidation	--	2.0
Cyc05	0.191	24	6.5	0.8	Shear	22	--
Cyc06	0.177	26	5.5	0.84	Reconsolidation	--	1.9
Cyc07	0.155	N/A	1.0	0.43	Reconsolidation	--	0.24
Cyc08	0.225	12	6.5	0.69	Shear	28	--

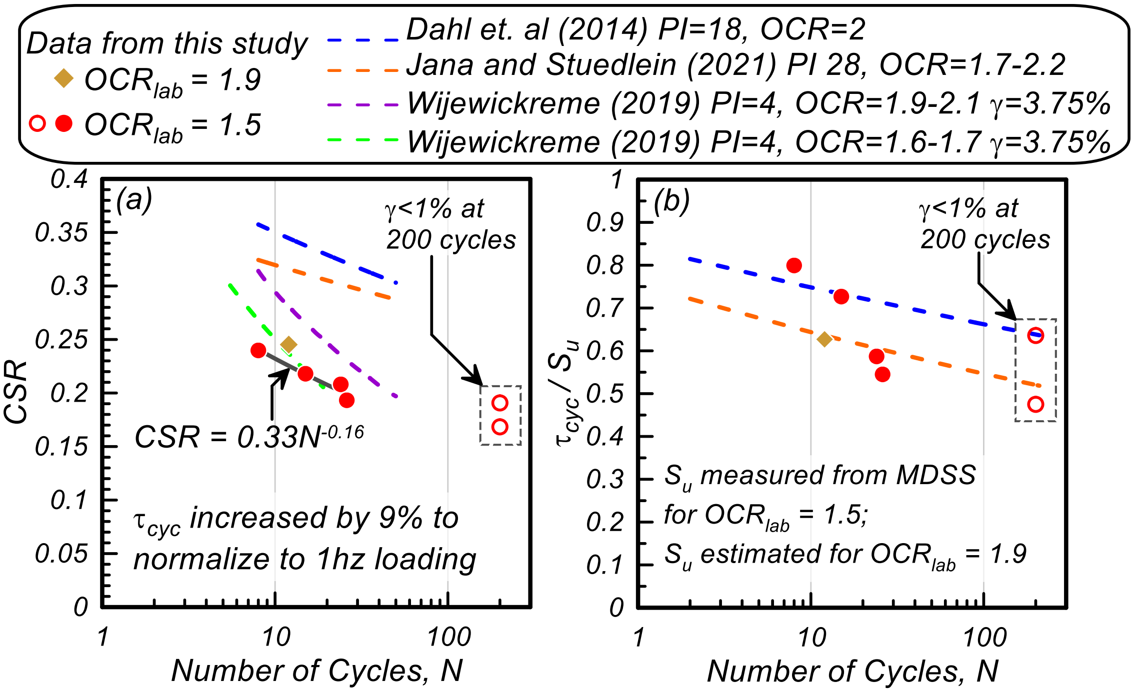

Figure 4: (a) CSR and (b) shear stress normalized by undrained shear strength compared to number of cycles to reach 3% S.A. shear strain

Post-Cyclic Reconsolidation.

Figure 5a displays the post-cyclic volumetric strains against the maximum (residual) r_u developed during cyclic testing, and then compared to trends presented in similar testing schedules of regional, geologically similar low-plastic silts (Jana and Stuedlein 2021, Wijewickreme et al 2019). This plot suggests that the data in this study (PI ranging between NP and 5) are bounded by the range proposed by Wijewickreme et al. (2019) which is developed for soils with PI ranging from 4 to 34 and plots slightly lower than the range proposed by Jana and Stuedlein (2021) which was developed for soils with PI of 28. Overall, the data confirms findings by other studies that the post-cyclic volumetric strains and settlement potentials in fine grained soils is strongly correlated with the pore water pressure ratio developed during cyclic loading. Figure 5b shows that post-cyclic volumetric strains are also strongly correlated with the maximum shear strain curing cyclic loading as suggested by other studies for sand soils (e.g. Ishihara and Yoshimine 1992).

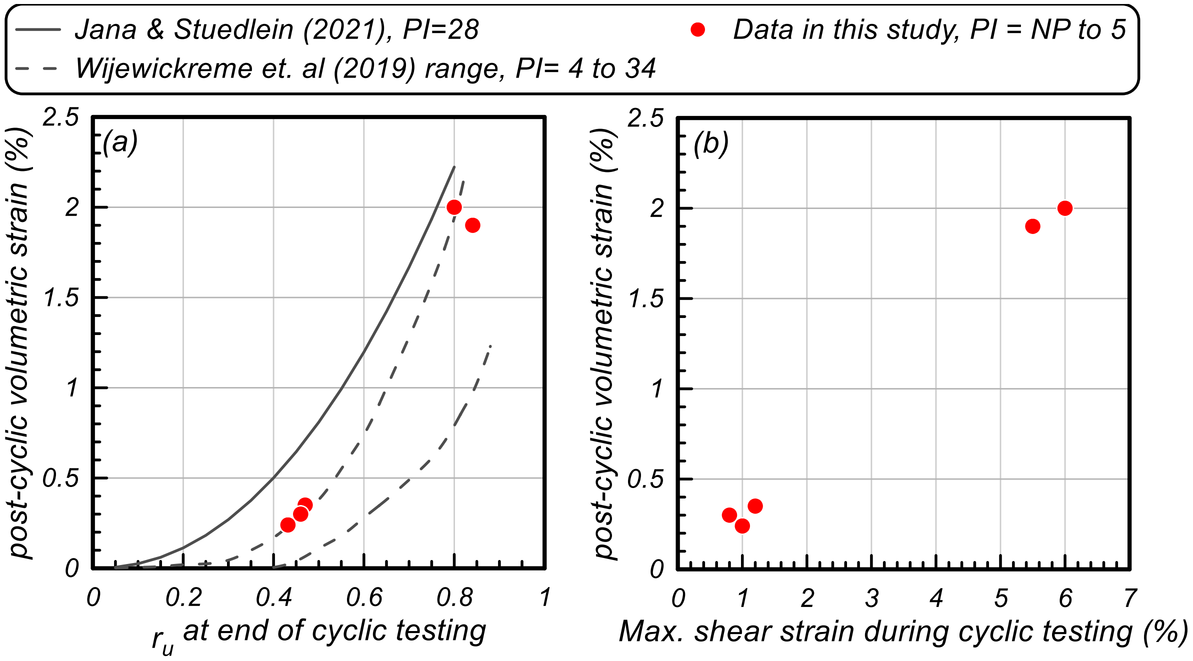

Figure 5: (a) post-cyclic volumetric strain compared to (a) maximum residual excess pore pressure during cyclic shear and (b) maximum shear strain during cyclic shear

Post-cyclic Undrained shear strength.

Figures 6a and 6b display the shear stress-strain relationship and stress load paths for static MDSS and post-cyclic MDSS tests. Figure 6c presents the post-cyclic shear stress, $\tau_{postcyclic}$, normalized by the corresponding static shear stress, τ_{static}, plotted against shear strain. While significant stiffness and strength degradation due to cyclic loading is observed at shear strains smaller than 5%, the specimens appear to regain their strength at shear strains larger than 10% due to a dilative response resulting in post-cyclic shear strengths that are 60% to 95% of the corresponding static undrained shear strength.

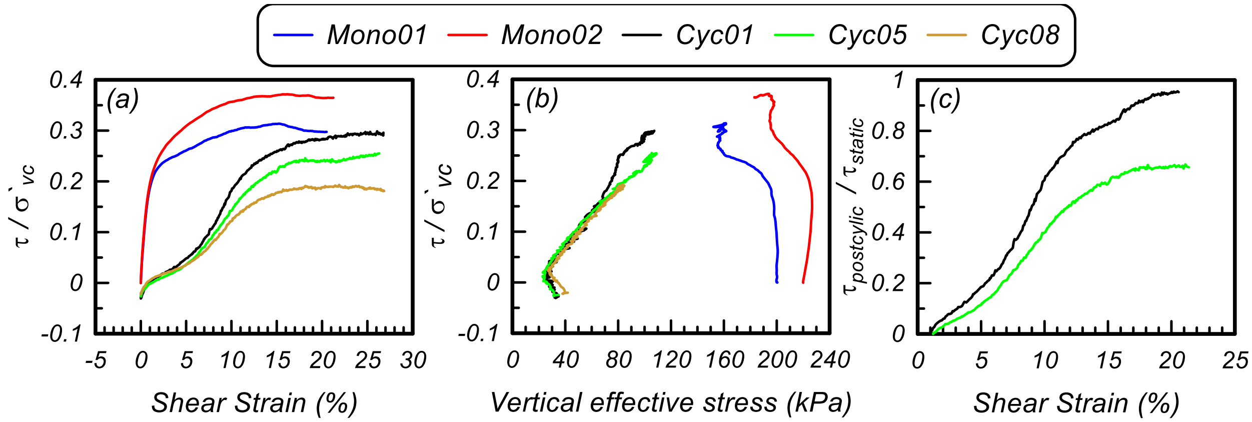

Figure 6: Static and Post-cyclic MDSS (a) Shear stress with strain (b) Shear stress with vertical effective stress and (c) post-cyclic shear stress normalized by static shear stress

2.4 Project Conclusions

A series of cyclic and monotonic shear tests were performed on intact soil specimens collected from Alluvial soils in Portland. The soils had PI ranging between NP and 5 and classify as liquefiable (sand-like behavior) using commonly used screening methods by Idriss and Boulanger (2008) and Bray and Sancio (2006). The cyclic tests were used to characterize the cyclic shear resistance and post-cyclic behavior of the soils. The soils in this test series tended to have sand-like cyclic behaviors, including liquefaction triggering and post-cyclic volumetric strains. The CRR of the soil was found to be 0.21 corresponding to 15 loading cycles as a reference. Post-cyclic volumetric strains ranged 0.3% to 2% and were found to be strongly correlated with r_u and maximum γ during cyclic loading. The post-cyclic volumetric strains followed trends presented in similar regional soils. The ratio of post-cyclic shear strength to static undrained shear strength was as low as 0.1 at a shear strain of 5% and increased to 60% to 95% at shear strains larger than 15%. Large uncertainties were observed in OCR estimations, due to the relative disturbance present in low-plasticity soil samples. The testing series presented contributes to the general body of knowledge regarding the behavior of low-plasticity silts during cyclic testing. While trends are noted, specific design values discussed including CRR, undrained shear strength, and post-cyclic volumetric strain are specific to the samples tested.

3.0 COMBINED EFFECTS OF LIQUEFACTION-INDUCED LATERAL SPREADING AND SUPERSTRUCTURE INERTIAL LOADS ON PILE FOUNDATIONS

3.1 Experimental setup

A full-scale shake table test was performed on a reinforced concrete (RC) pile subjected to liquefaction-induced lateral spreading at the University of California, San Diego. Full details on the experiment are provided in Ebeido (2019). Figure 7 shows the experimental configuration, including the thicknesses of the different soil layers. The RC pile was 0.25 m in diameter and 3.7 m in length, and it included six #3 longitudinal reinforcement bars with a 2.5-cm concrete cover and #3 spiral bars spaced at a distance of 20 cm. The 28-day compressive strength of concrete (f'c) was 16 MPa. The tip of the pile was firmly attached to the shake table to represent an embedment into a firm bearing layer under field conditions. The superstructure was comprised of two concrete masses (Superstructures A and B), which produced the inertial load on the foundation during shaking in addition to the self-weight of the concrete pile. The instrumentation included porewater pressure transducers, strain gauges, pressure transducers (at the soil–pile interface), accelerometers, and linear voltage displacement transducers (LVDTs). The pile was oriented vertically; however, the laminar shear box and the soil surface were on a 4-degree incline. The laminar shear box approximated the free-field conditions by allowing the soil to deform in shear with minimal restraint from the external boundary. At the pile location, the soil strata consisted of approximately 0.8 m of dry dense sand (with an estimated relative density D_R of 70%) over 0.7 m of saturated loose sand (with an estimated D_R of 30%) over 1.3 m of saturated dense sand (with an estimated D_R of 70%). The water table was approximately 0.8 m below the ground surface. Figures 8a and 8b show side views of the laminar shear box at the beginning and end of the test, respectively, while Fig. 8c shows the top view of the superstructure masses.

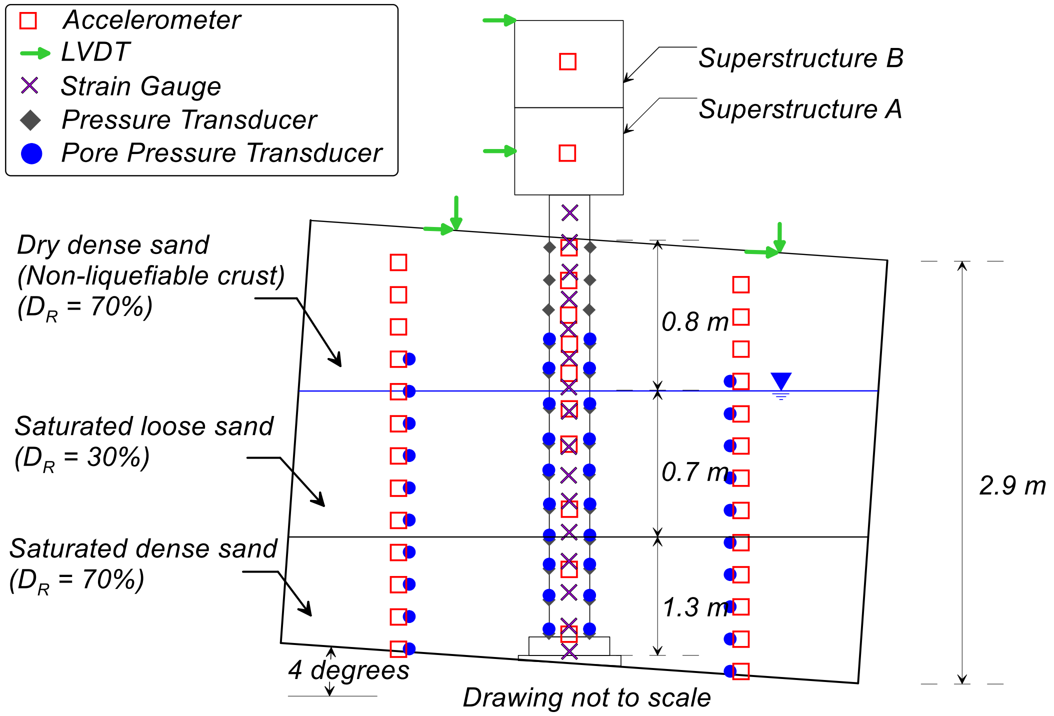

Figure 7. Experimental setup and sensor locations.

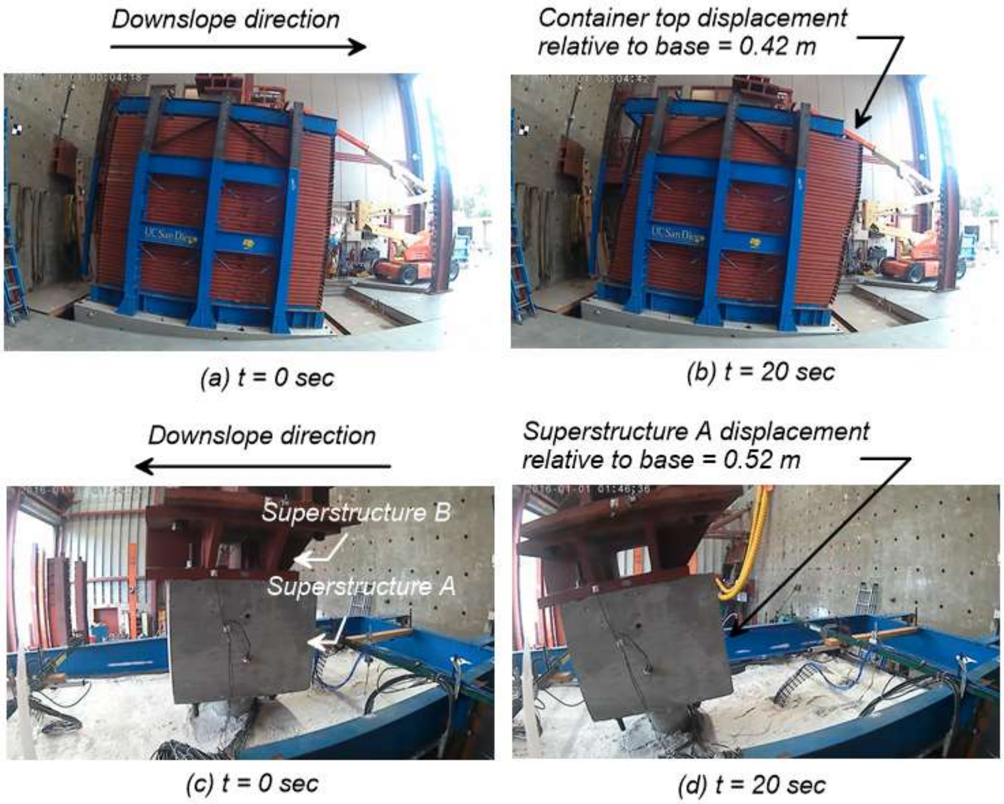

Figure 8. Side and top views of the model at the beginning (a,c) and end of the test (b,d).

3.2 RESULTS

Overall Pile and Soil Responses

Time histories of the soil and pile shaking response are shown in Figure 9, and a schematic to the right of each subfigure shows the location of the plotted instrumentation recording. Pile head and soil ground surface displacements are shown in Fig. 9a. The plotted pile head displacements were recorded at Superstructure A, while soil displacements were recorded at the ground surface at an approximate distance of 1 m from the pile in the downslope direction (in line with the pile). Representative porewater pressure ratios R_u (defined as the cyclically induced excess porewater pressure divided by the initial vertical effective stress) for the loose and dense saturated sand units are shown in Fig. 9b, as measured by porewater pressure transducers placed at depths of 0.99 m and 2.09 m, respectively. The acceleration time histories at the base of the shake table and at Superstructure A are shown in Fig. 9c. The base acceleration is a sinusoidal wave that ramps up to a maximum amplitude of 0.16 g applied at a constant frequency of 2 Hz (a period of 0.5 sec) and then ramps down to zero acceleration. The natural frequency of the superstructure is approximately 1.7 Hz (a natural period of 0.6 sec), which was determined based on the maximum amplification of the spectral acceleration of the superstructure with respect to the spectral acceleration of the base. The superstructure acceleration is used in this study to represent the inertial load on the foundation.

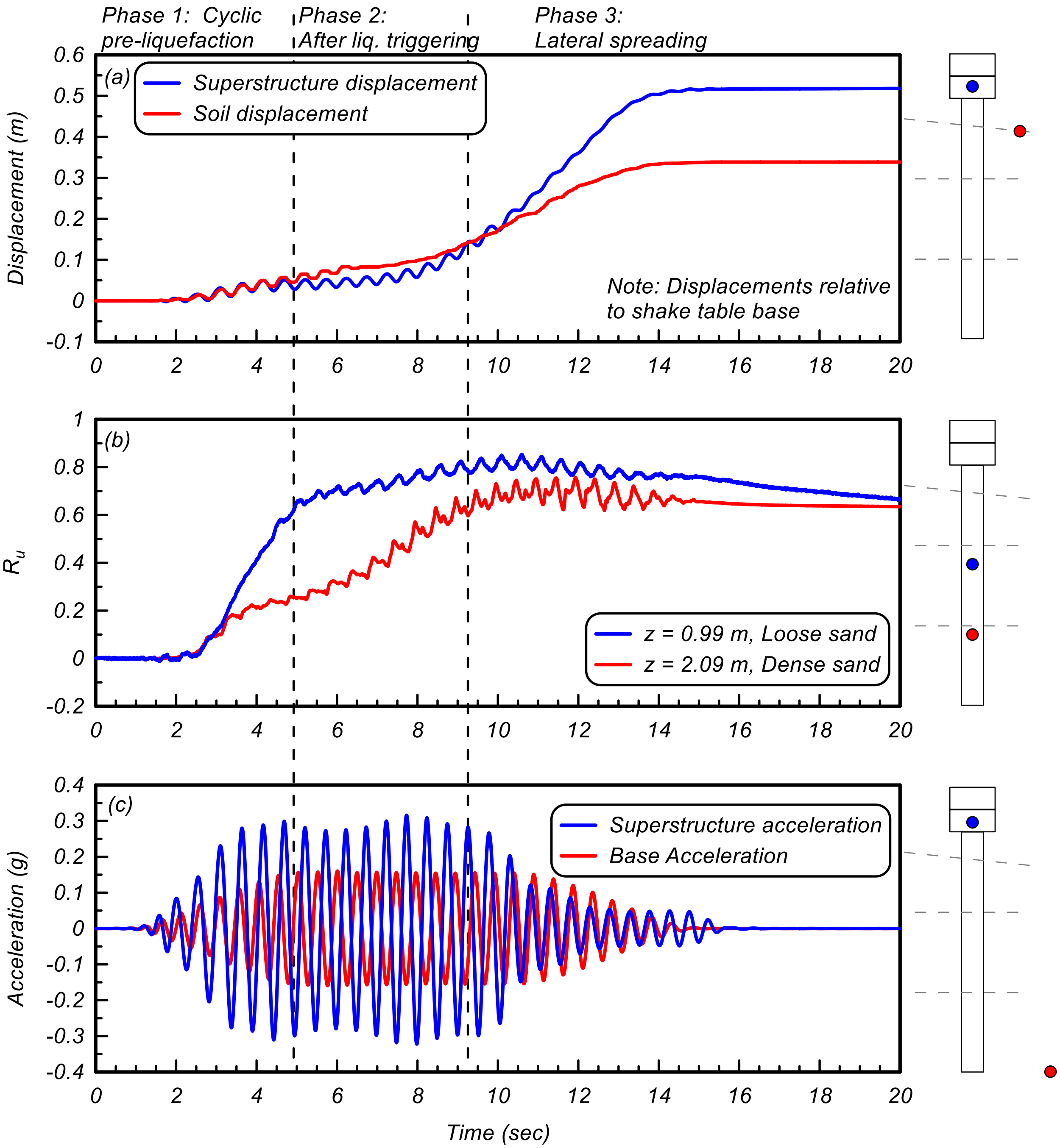

Figure 9. Time histories of (a) pile and soil displacements, (b) porewater pressure ratios in loose and dense sand layers, and (c) base and superstructure accelerations.

The cyclic response of the soil and pile were categorized into three phases that represent different mechanisms of inertial and kinematic load interactions. These phases (which are indicated in Fig. 3 using vertical dashed lines) can be summarized as follows:

- Phase 1 – Cyclic response pre-liquefaction. This phase corresponds to the first 5 sec of the motion, during which the superstructure exhibited strong inertial cycles and the porewater pressures within the loose and dense saturated sand layers were small (i.e., $R_u < 60\%$).

- Phase 2 – Cyclic response after liquefaction was triggered. This phase occurs between approximately 5 sec and 9.2 sec, when the loose sand was liquefied, resulting in the accumulation of soil displacements accompanied by large inertial cycles. The calculated maximum R_u values did not reach 100%, which was likely due to the uncertainties in estimating the initial vertical effective stress and the exact depth of the embedded sensors. However, the rapid accumulation of soil displacements during this phase indicates that liquefaction was triggered.

Phase 3 – Lateral spreading. This phase occurs after 9.2 sec, when both the loose saturated sand and the upper portion of the dense saturated sand were liquefied, resulting in a significant accumulation of soil displacement and several strong inertial cycles, followed by decaying inertial cycles. A plastic hinge formed at the base of the pile at approximately 9.2 sec, resulting in significant accumulation of deformations at the pile head during the lateral spreading phase. The superstructure acceleration began to decrease before the base acceleration started to taper off, which is attributed to (a) the isolating effect of the liquefied soils in transmitting the input energy upwards to shallower soils and the superstructure, and (b) yielding of the pile at the base.

Kinematic Loads from Nonliquefiable Crust

In this study, the normal soil reactions within the dry (nonliquefiable) crust are presumed to be representative of kinematic loads on the pile due to liquefaction-induced lateral ground deformations. The normal soil reactions in this study refer to the perpendicular pressures at the soil–pile interface and were directly measured using two arrays of pressure transducers that were mounted on the upslope and downslope sides of the pile. Figure 10 shows the maximum soil reactions along the pile measured from the upslope pressure transducer array (maximum positive) and the downslope pressure transducer array (maximum negative) during the entire ground motion. The sign convention used for the normal pressures follows the same sign convention that is used for all other measurements presented in this paper: pressures applied to the pile in the downslope direction (registered by the pressure transducer array attached on the upslope side of the pile) are positive, and pressures in the upslope direction (registered by the pressure transducer array attached on the downslope side of the pile) are negative. As shown in this figure, the largest pressures were registered by pressure transducers at a depth of 0.33 m; in this study, these pressures are considered to be representative of kinematic loads from the crust and are used to determine the relative contribution of inertial and kinematic demands during the critical cycles.

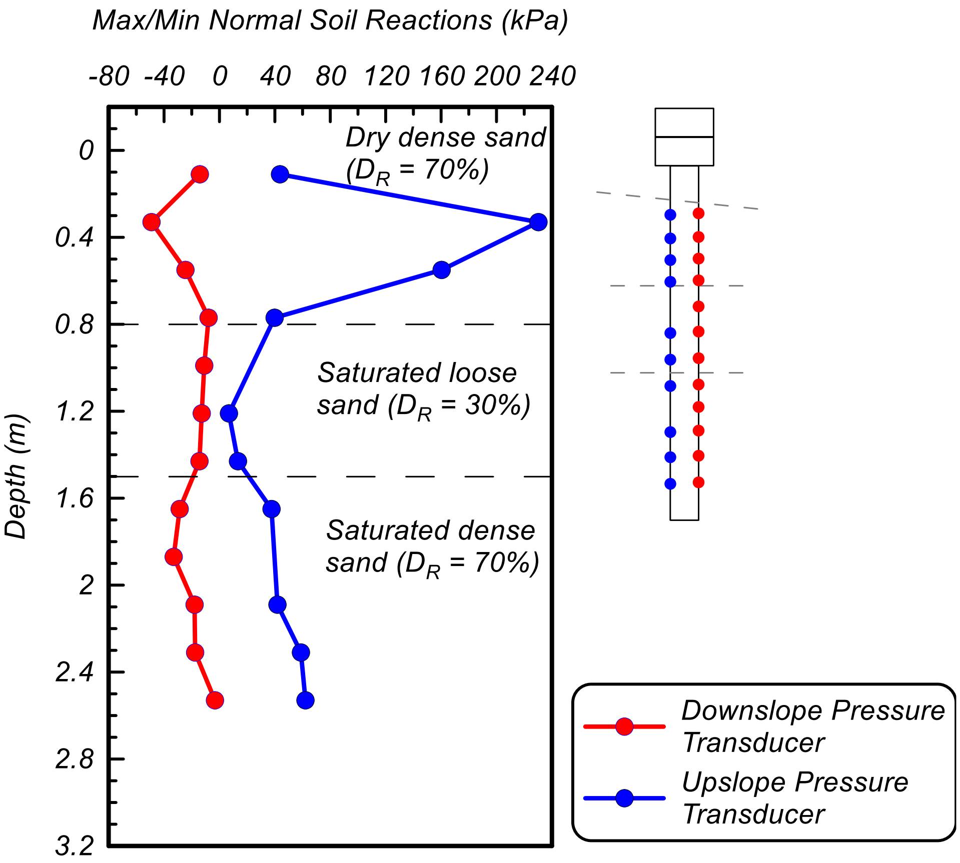

Figure 10. Profile of maximum and minimum normal soil reactions along the pile during the ground motion.

Figure 11a shows the time histories of normal soil reactions at the two pressure transducers installed at a depth of 0.33 m. Fig. 11b shows the time history of the resultant normal soil reactions from both pressure transducers at a depth of 0.33 m. The positive soil reactions in Fig. 11a show the normal stress applied in the downslope direction, which was registered by the pressure transducer installed on the upslope side of the pile. The negative soil reactions in Fig 11a correspond to the normal pressure applied in the upslope direction, as registered by the pressure transducer installed on the downslope side of the pile. The pressure transducer on the downslope side did not register any pressure after approximately 3.8 sec; this is attributed to the formation of a gap on the downslope side of the pile. The gap was formed on the downslope side of the pile because the soil displacements exceeded the pile displacement during Phase 2 (between 5 sec and 9.2 sec) as shown in Fig. 9a.

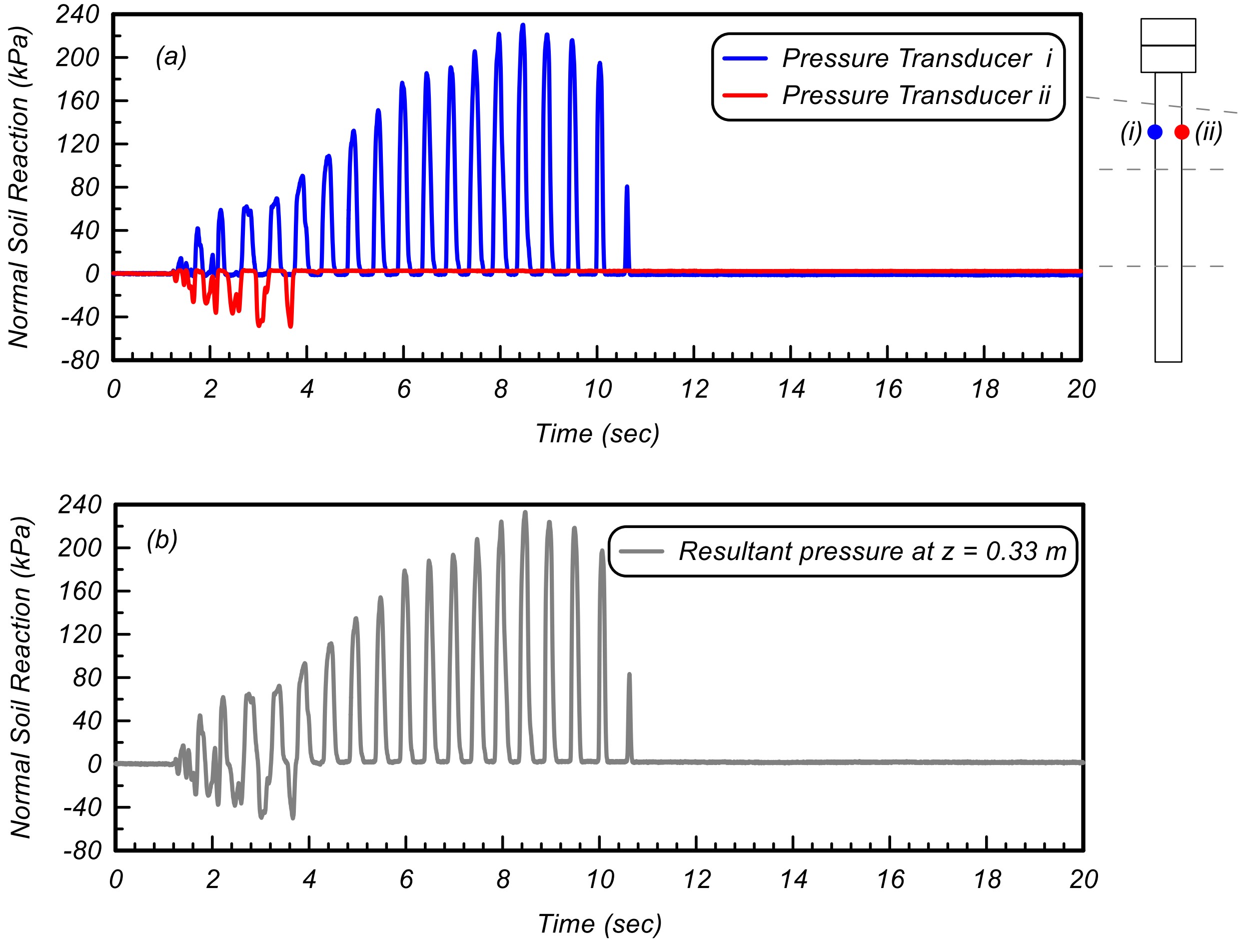

Figure 11. Time histories of (a) soil reactions in the upslope and downslope faces of the pile at a depth of 0.33 m and (b) resultant normal soil reactions at a depth of 0.33 m.

Load Transfer Mechanism between Pile and Nonliquefiable Crust

The load transfer mechanism between the pile and the nonliquefiable crust is examined using the normal pressures registered on the upslope and downslope faces of the pile during Phase 2 after liquefaction was triggered. Figure 12a shows the time histories of the pile head and soil displacements during Phase 2 (between 5 sec and 10 sec). The pile head displacement is measured at Superstructure A, and the soil displacement is measured using an LVDT that was attached to the ground surface at a distance of approximately 1 m from the pile in the downslope direction (in-line with the pile). Fig. 12b shows the acceleration at Superstructure A, and Fig. 12c shows the normal soil reactions from the two pressure transducers placed at a depth of 0.33 m during the same timeframe. The soil and pile responses are examined at two moments in time:

- At t = 7.47 sec, the pile head swings upslope as indicated by the local minimum in the pile head displacement in Fig. 12a and a negative acceleration (inertia) in Fig. 12b.

- At t = 7.73 sec, the pile head swings downslope as indicated by the local maximum in the pile head displacement in Fig. 12a and a positive acceleration (inertia) in Fig. 12b.

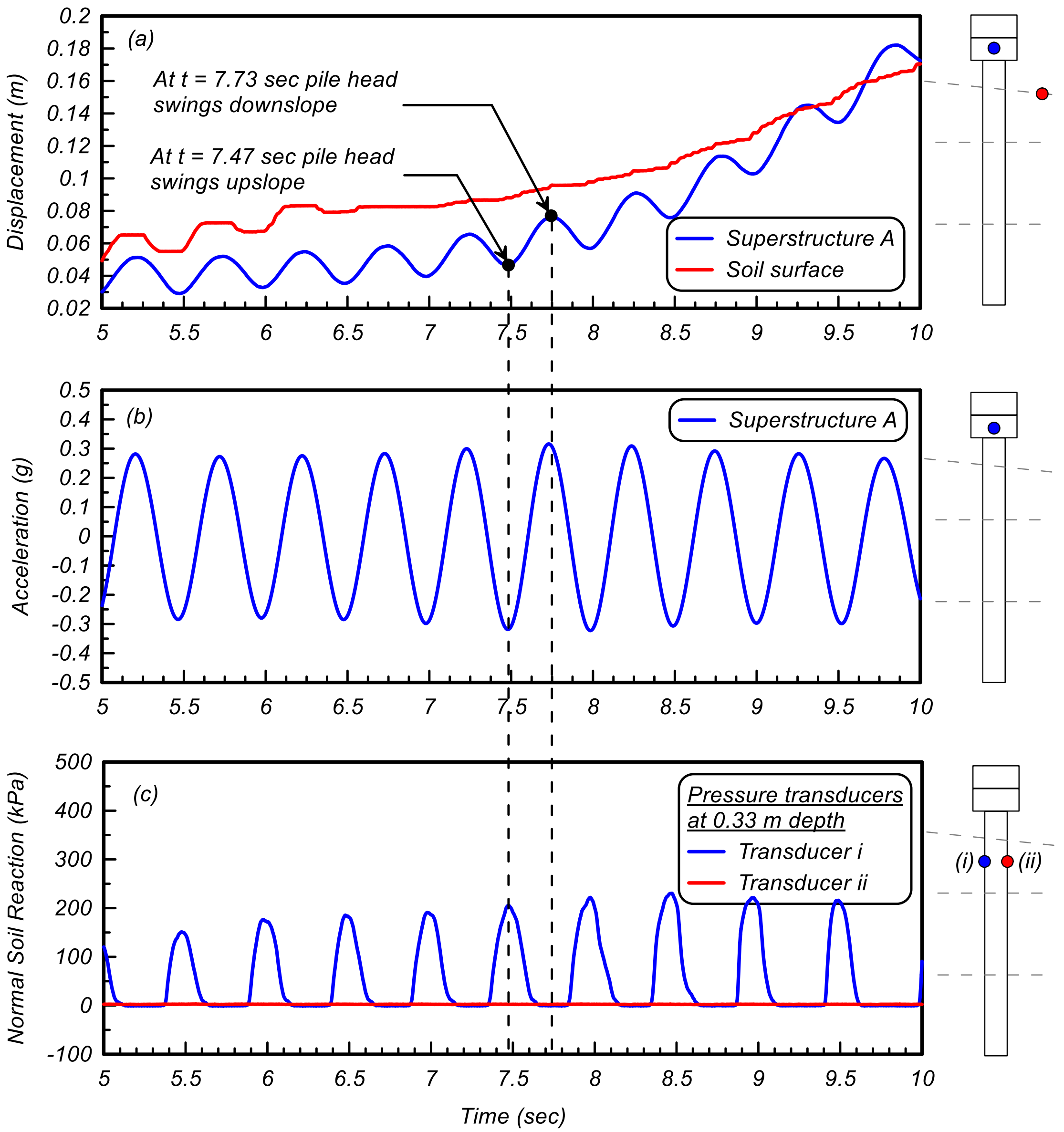

Figure 12. Time histories of (a) soil and pile head displacements, (b) pile head acceleration, and (c) normal soil reactions at a depth of 0.33 m.

As can be seen from Fig. 12c, when the pile swings in the upslope direction (*t* = 7.47 sec), the crust applies downslope pressure on the pile. As the inertial load changes sign and pushes the pile head in the downslope direction (*t* = 7.73 sec), no normal pressure is registered in either the downslope or upslope faces of the pile. The lack of pressure on the downslope side of the pile at *t* = 7.73 sec is attributed to the formation of a gap on the downslope side of the pile, when the soil displacements exceeded the pile displacements. The lack of pressure on the upslope side of the pile (i.e., zero lateral spreading force) at *t* = 7.73 sec is attributed to the pile outrunning the soil during the downslope inertial cycles. This response is further illustrated in Figures 13a and 13b, which show the profiles of the soil and pile displacements at t = 7.47 sec and t = 7.73 sec, respectively. The container displacements in this figure are recorded using LVDTs attached along the height of the laminar box and are assumed to approximately represent the free-field soil displacements. The two soil displacements at the ground surface are measured using two LVDTs attached to the soil surface at two locations: one LVDT was placed approximately 0.8 m upslope from the pile, and the other was placed approximately 1 m downslope from the pile (in line with the pile). These two soil displacements are smaller than the container (free-field) displacement because they are affected by the presence of the pile (i.e., the “pile-restrained” soil displacements mentioned in Caltrans 2012). The displacements at Superstructures A and B were recorded using LVDTs. The pile deformation with depth (indicated by a dashed line in Figs. 13a and 13b) is approximated as a reference to facilitate a comparison to the soil displacements. This figure clearly shows that even though the soil displacements have not yet reached their maximum permanent values at the end of motion, they are large enough during the cyclic response after liquefaction was triggered (Phase 2) that they exceed the pile displacements, resulting in the formation of a gap on the downslope side of the pile.

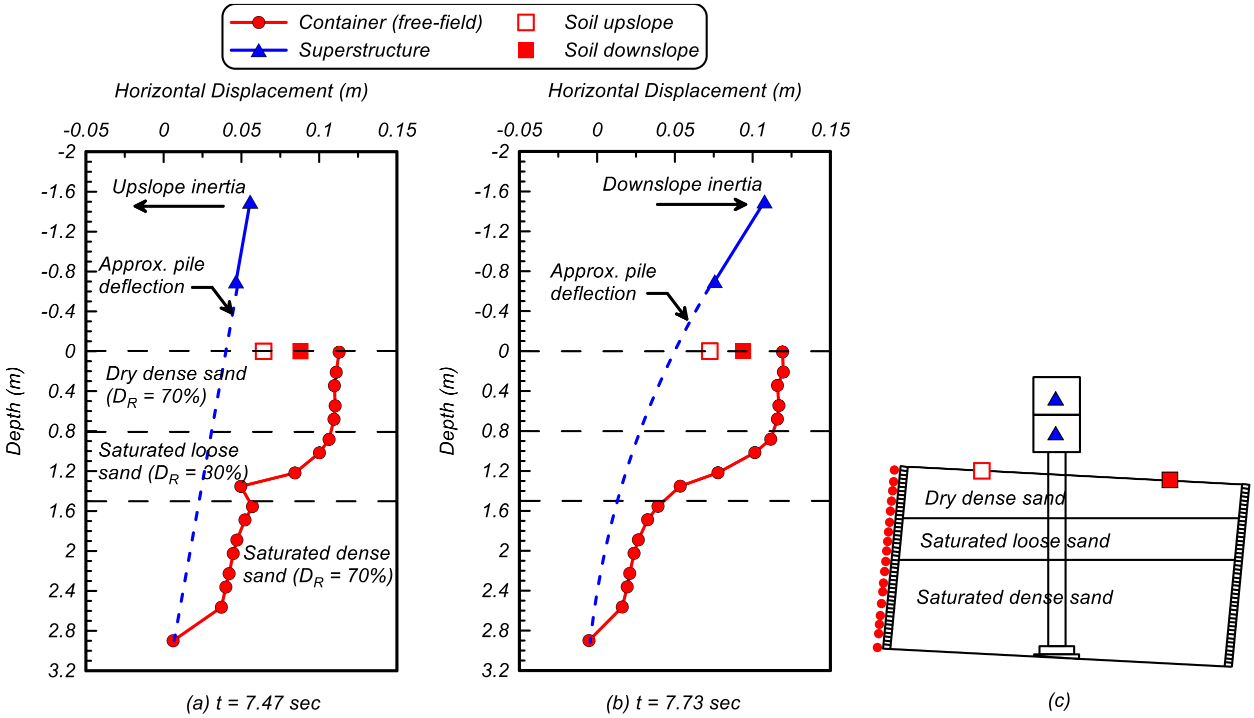

(a) t = 7.47 sec

(b) t = 7.73 sec

(c)

Figure 13. Horizontal displacements of the soil and pile head at (a) t = 7.47 sec and (b) t = 7.73 sec. (c) Location of the LVDT sensors.

The normal pressure profiles are plotted in Figures 14a and 14b at *t* = 7.47 sec and *t* = 7.73 sec, respectively. While the kinematic load from the nonliquefiable crust is positive (in the downslope direction) when the pile swings in the upslope direction (*t* = 7.47 sec), the crust load vanishes as the superstructure inertia swings the pile in the downslope direction (*t* = 7.73 sec). This finding is significant, as it suggests that the crust load and inertial load are out of phase when the pile moves in the upslope direction and that there is no crust load (either driving or resisting) as the pile outruns the soil when moving in the downslope direction. The interaction of the inertial and kinematic crust loads are discussed in greater detail in the following section.

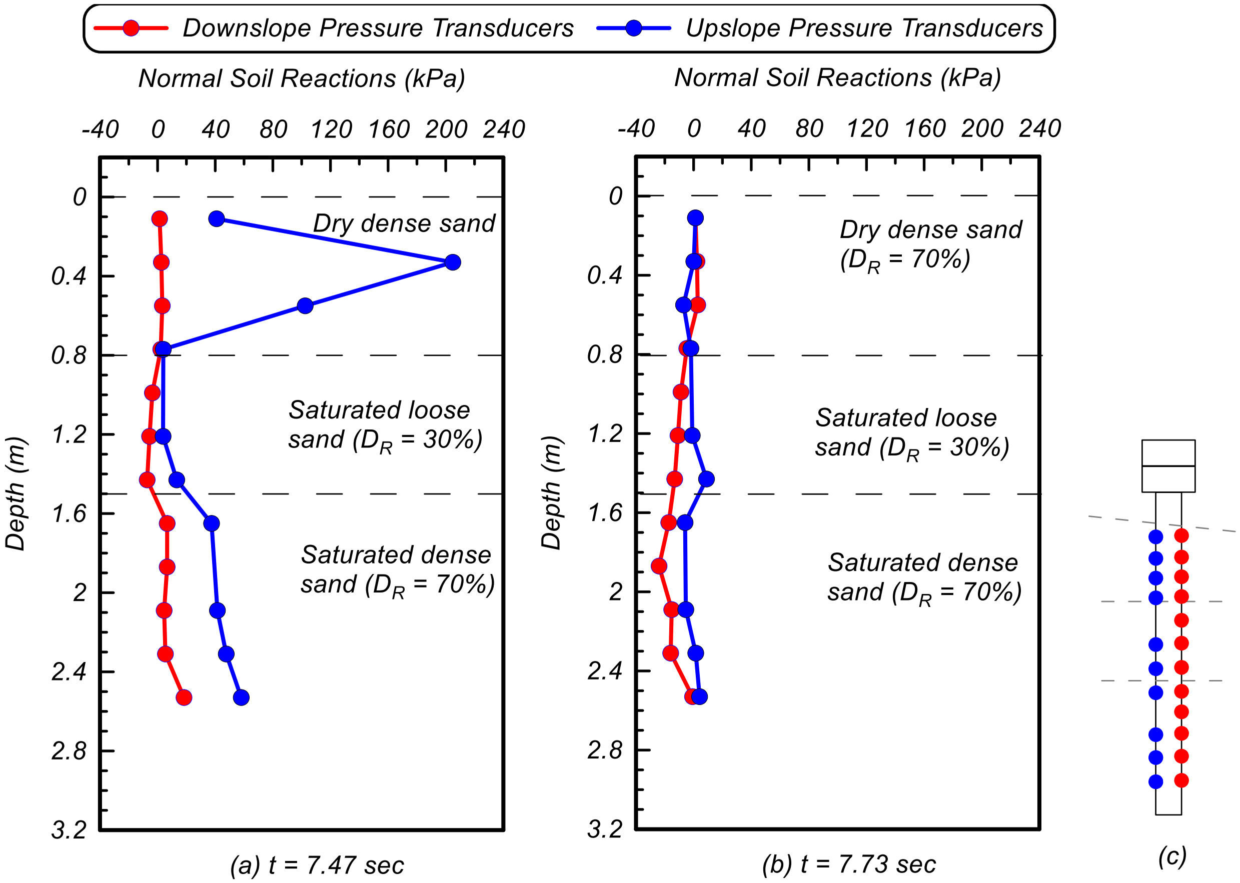

(a) *t* = 7.47 sec

(b) *t* = 7.73 sec

(c)

Figure 14. Profiles of normal soil reactions at (a) *t* = 7.47 sec and (b) *t* = 7.73 sec. (c) Location of the load cells.

Load vs. Displacement Relationship in Nonliquefiable Crust

Figure 15 shows the relationship between the normal soil reaction and the relative displacement between soil and pile within the crust. The soil reaction is calculated as the resultant of the normal pressures from the two load cells attached on the upslope and downslope faces of the pile at a depth of 0.33 m (shown in Fig. 11b). The relative displacement between the soil and pile is calculated by subtracting the recorded displacement from the LVDT attached to the container frame at a depth of 0.33 m (representative of the free-field soil displacement) from the displacement recorded by the LVDT attached to Superstructure A, which is scaled down by a factor of 0.7 to approximate the pile displacement at a depth of 0.33 m (this factor is estimated using the dashed lines shown in Fig. 13). The unloading cycles in this relationship correspond to half cycles where the downslope inertia displaces the pile head in the downslope direction. The half loading cycle between 7.47 sec and 7.73 sec is shown in Fig. 13 as a reference. As explained earlier, the unloading of the crust load is associated with the pile outrunning the soil due to the downslope inertia, causing the pile to deform into a gap that has formed on the downslope side of the pile. Figure 16a shows a photo of the model at *t* = 7.47 sec, when the gap in the downslope front of the pile is clearly visible. At that time, the pile head inertia pushes the pile head in the upslope direction. Fig. 10b shows the model at *t* = 7.73 sec, when the downslope inertia pushes the pile head in the downslope direction. The gap that is visible at this time is an indication that the gap had not closed, despite the movement of the pile into the gap, resulting in zero soil pressure from the crust on both the upslope side and the downslope side of the pile.

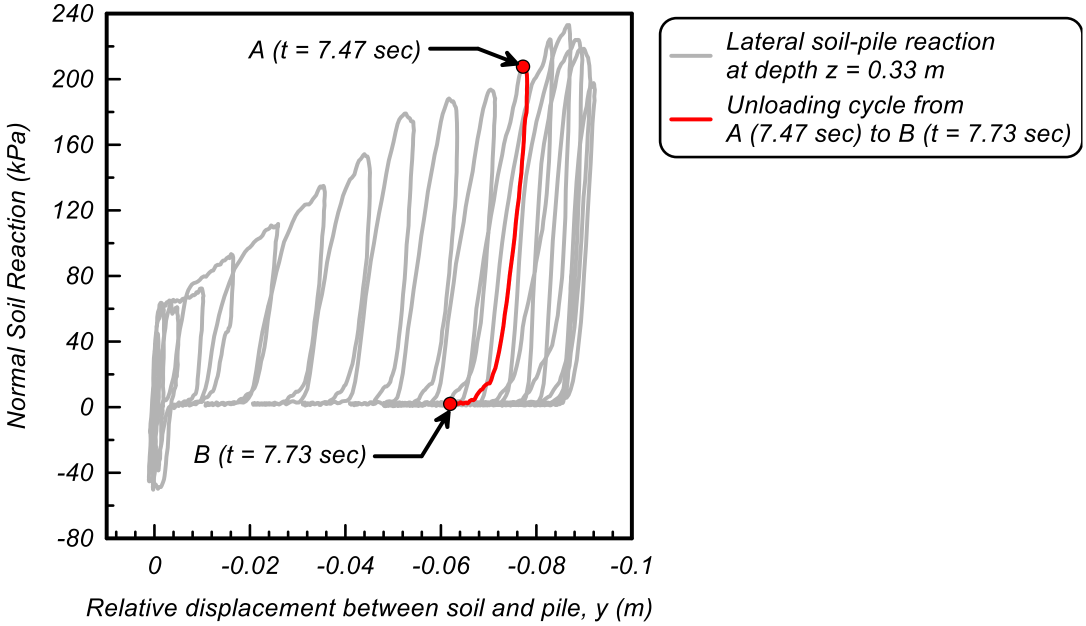

Figure 15. Relationship between soil reactions and relative displacements between the soil and pile within the nonliquefiable crust at a depth of 0.33 m.

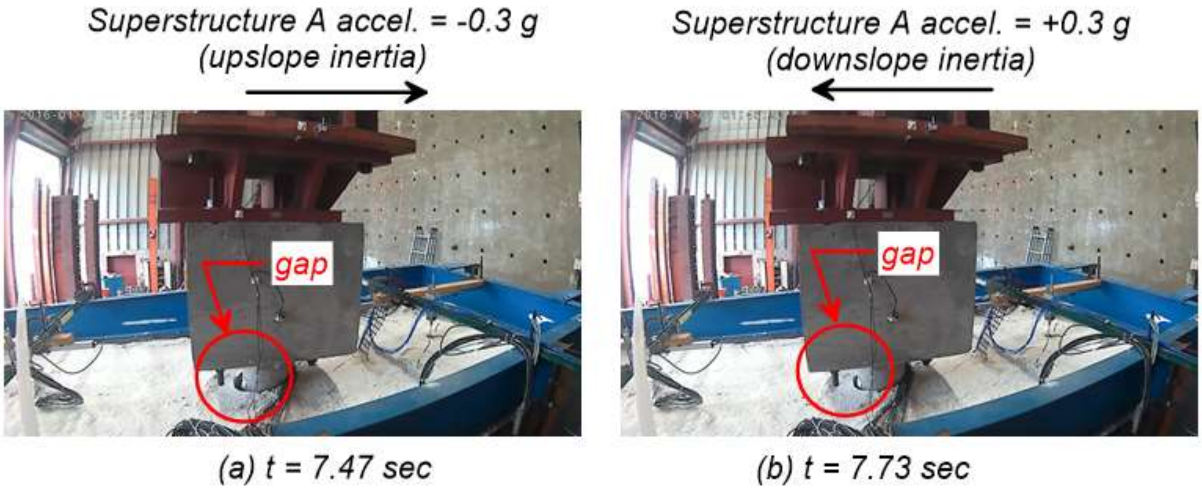

Figure 16. Gap formation on the downslope side of the pile at (a) *t* = 7.47 sec and (b) *t* = 7.73 sec.

Interaction of Inertial and Kinematic Demands at Peak Inertial Loads

The interaction of inertial and kinematic demands is quantified by extracting the kinematic loads at the time of peak (or close to peak) inertial loads to provide a relative comparison to the design guidelines that recommend combining full inertial loads with a fraction of the lateral spreading loads (e.g., POA 2017 in Table 1). The pile head acceleration at Superstructure A (shown previously in Fig. 9c) is considered as a representative of inertial load, and the resultant normal pressure at a depth of 0.33 m within the nonliquefiable crust (shown previously in Fig. 11b) is used as a representative of kinematic load. The time histories of inertial and kinematic loads are replotted in Figure 17a along with the critical times when the pile head acceleration is at its local maxima (i.e., the superstructure is moving in the downslope direction) and minima (i.e., the superstructure is moving in the upslope direction). The normalized inertial and kinematic loads (I and K), which are calculated as the inertial and kinematic loads extracted at the critical times normalized by their corresponding peak values during the ground motion, are plotted for downslope cycles and upslope cycles in Figs. 17b and 17c, respectively. The peak acceleration (inertia) was 0.32 g, and the peak kinematic load was 233 kPa. The interactions of I and K are discussed below for the three phases indicated in Fig. 9. Histogram bar plots are provided for the critical times.

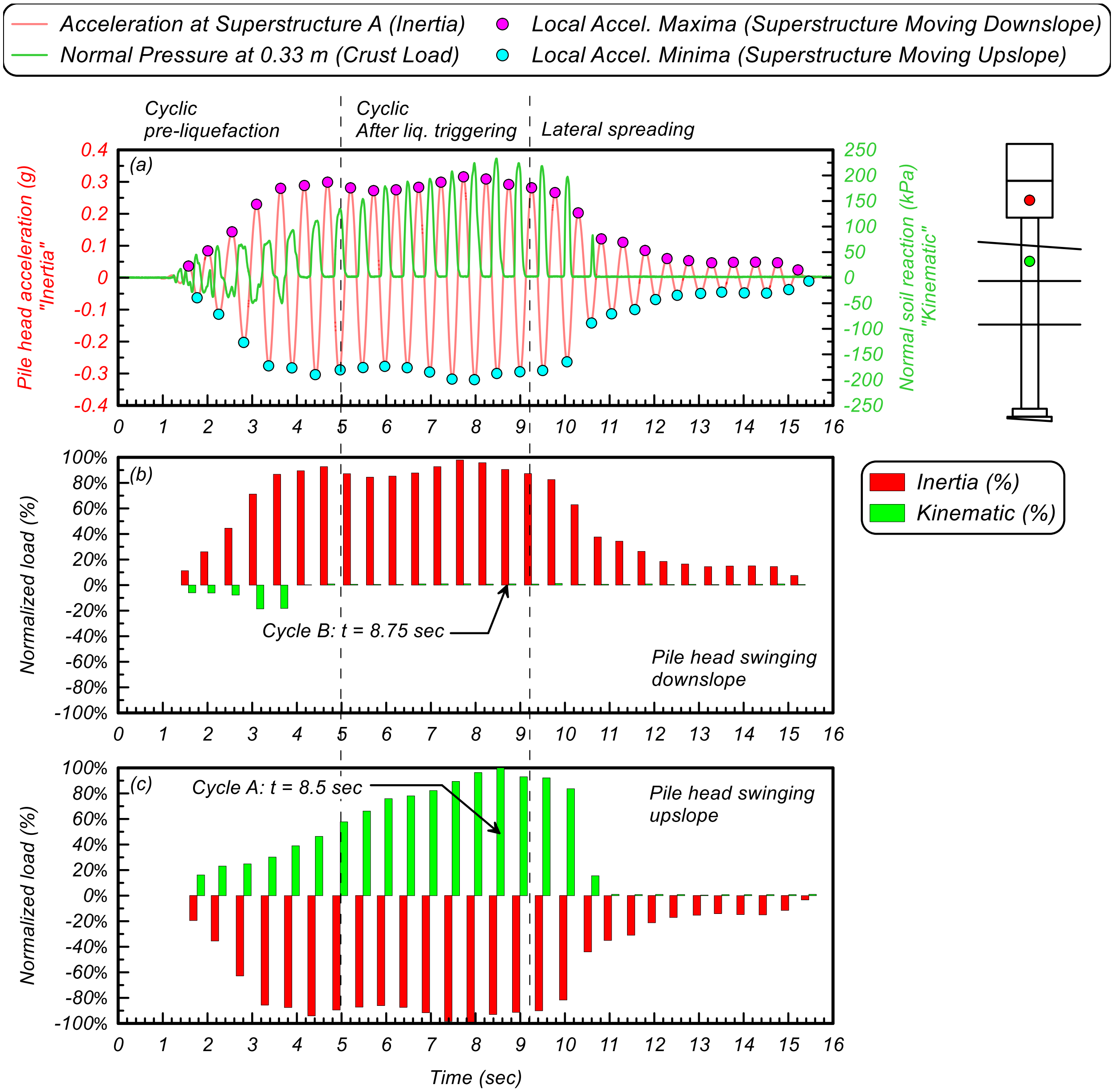

Figure 17. (a) Pile head acceleration and normal soil reaction at a depth of 0.33 m within the nonliquefiable crust. (b) Normalized inertial and kinematic loads during downslope cycles. (c) Normalized inertial and kinematic loads during upslope cycles.

During Phase 1 (between 0 and 5 sec), the loose sand has not yet liquefied, and the dynamic response of the pile is primarily driven by the inertial load with lateral resistance from the crust: during upslope inertial cycles (where *I* has a negative value), the crust load is positive and is resisting the pile movement. Similarly, during the downslope inertial cycles (where *I* has a positive value), the crust load is negative and is also resisting the pile movement.

During Phase 2 (between 5 sec and 9.2 sec), the loose saturated sand layer has liquefied, resulting in incremental accumulation of soil displacements in the downslope direction. The upslope inertial cycles (negative *I*) during this phase are accompanied by resisting crust loads (positive *K*). However, the downslope inertial cycles (positive *I*) are met with no resisting or driving loads from the crust. In this figure, Cycle A ($t = 7.47$ sec) and Cycle B ($t = 7.73$ sec) correspond to the critical times when the inertia is at maximum. Detailed soil and pile responses at these two critical times were presented earlier in Fig. 13.

During Phase 3 (after 9.2 sec), the underlying saturated dense sand has liquefied, resulting in a significant accumulation of soil displacements (i.e., lateral spreading). The pile connection at the base yielded at 9.25 sec, resulting in the formation of a plastic hinge at the base and excessive deformations at the pile head. The pile head acceleration is significantly reduced after this time; this behavior is attributed to the isolating effects of the softened liquefied soils and the yielded pile, which reduce the motion energy that is transmitted to the superstructure. After pile failure, a significant reduction in the crust load (*K*) is observed both in upslope cycles and the downslope cycles; this finding is likely due to the reduced flexural resistance in the failed pile. Considering that most piles are designed to be capacity protected (i.e., no plastic hinge is allowed to form in pile), the I and K load combination exhibited in this phase should not be considered in the design. Table 6 lists the previously described proportional I and K at the selected cycles (Cycles A and B) as well as the porewater pressure ratios in the liquefiable sand layers.

Table 6: Proportional *I*, *K*, and R_u at select critical cycles corresponding to peak inertia

Cycle	Time (sec)	I^a	K^a	R_u in Loose Sand	R_u in Dense Sand
A	7.47	−98%	+89%	0.76	0.48
B	7.73	+98%	+1%	0.73	0.45

[a] Positive values indicate the downslope direction; negative values indicate the upslope direction.

Interaction of Inertial and Kinematic Demands at Peak Pile Strains

From a design perspective, it is important to evaluate the proportional inertial and kinematic interaction factors (i.e., *I* and *K*) with respect to the structural demands on piles. In this study, the pile strains were recorded by strain gauges attached to the reinforcing bars on two opposing (upslope and downslope) sides of the pile. Pile curvatures were calculated using the difference in strains from two opposing strain gauges at a given depth divided by the distance between the two stain gauges (i.e., 0.18 m). Calculating the bending moments from strain gauge data is challenging when the pile exhibits nonlinear behavior. Therefore, in this study, pile strains and curvatures are directly used as a measure of pile demand.

Figure 18a shows the profiles of maximum and minimum pile strains recorded in both the upslope and downslope strain gauge arrays. The missing data points correspond to a few strain gauges that malfunctioned during the test. Fig. 18b shows the maximum and minimum pile curvature. The maximum (positive) curvature and minimum (negative) curvature occur at depths of 1.89 m and 0.49 m, respectively.

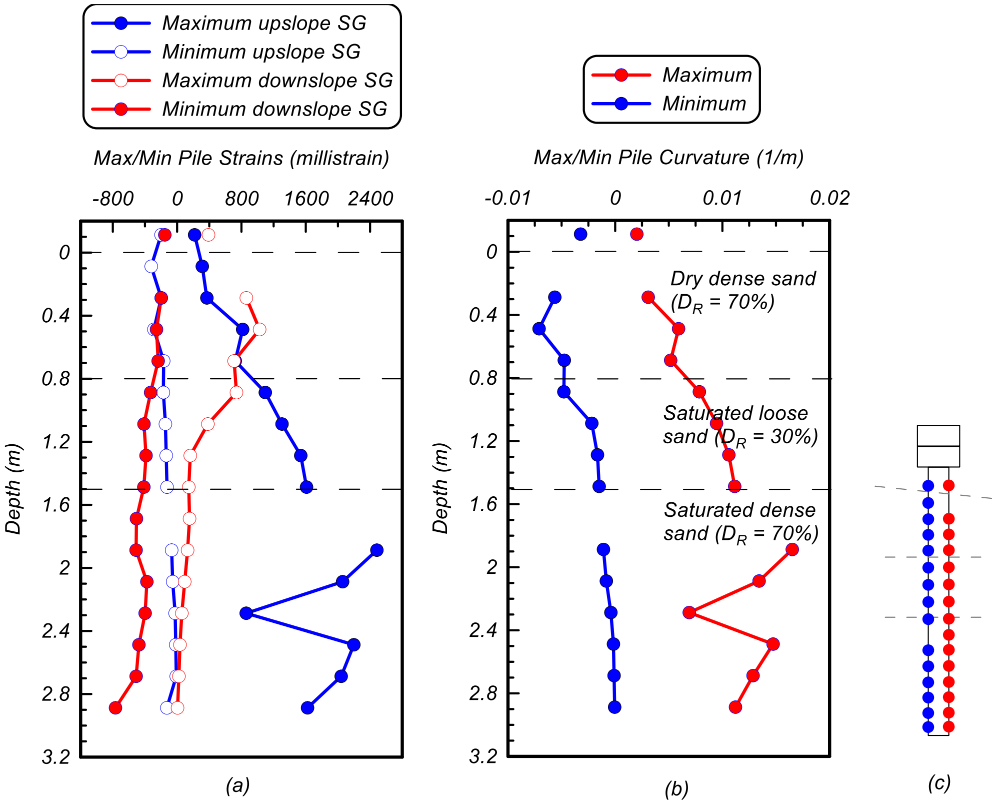

Figure 18. Profiles of (a) maximum and minimum pile strains and (b) maximum and minimum curvature. (c) Location of strain gauges along the pile.

Figures 19a and 20a show the time histories of strains in the two strain gauges placed at a depth of 0.49 m (SG13 and SG29) and two strain gauges placed at a depth of 1.89 m (SG6 and SG22), respectively. Both figures show that large pile strains developed during Phase 2 after liquefaction was triggered. Fig. 13a shows that the maximum (positive) strain at a depth of 0.49 m is registered in the strain gauge that is attached to the upslope side (SG13); this implies that the peak pile strains occur when the pile head swings in the upslope direction. Similarly, Fig. 14a shows that the maximum (positive) strain at a depth of 1.89 m is registered in the strain gauge attached to the downslope side (SG22); this implies that the peak pile strains occur when the pile head swings in the downslope direction. Figs. 19b and 20b show the proportional inertial and kinematic loads (i.e., *I* and *K*) at the critical times when the pile strains are at peak at depths of 0.49 m and 1.89 m, respectively. The results presented in these two figures confirm the same characteristics for *I* and *K* that were observed previously in Fig. 17:

Large pile strains at a shallow depth (0.49 m) are primarily driven by the inertial load and are recorded during cycles where the pile head was swinging in the upslope direction. During these cycles, the inertial and kinematic loads were out of phase. At the critical time when the pile strain is close to maximum (t = 7.98 sec), the inertial load is at maximum in the upslope direction (I = −100%), and the crust applies a resisting load in the downslope direction (K = +96%).

Large strains at a deeper location (1.89 m) were recorded during the cycles where the pile head was swinging in the downslope direction. During these cycles, the inertial load was met with no kinematic load from the crust, which was likely due to the pile head outrunning the soil displacement and deforming the pile into a gap that had formed at the front of the pile. At the critical time when the pile strain is at maximum (t = 7.70 sec), the inertial load is close to maximum in the downslope direction (I = +91%), and the kinematic crust load is negligible (K = +1%).

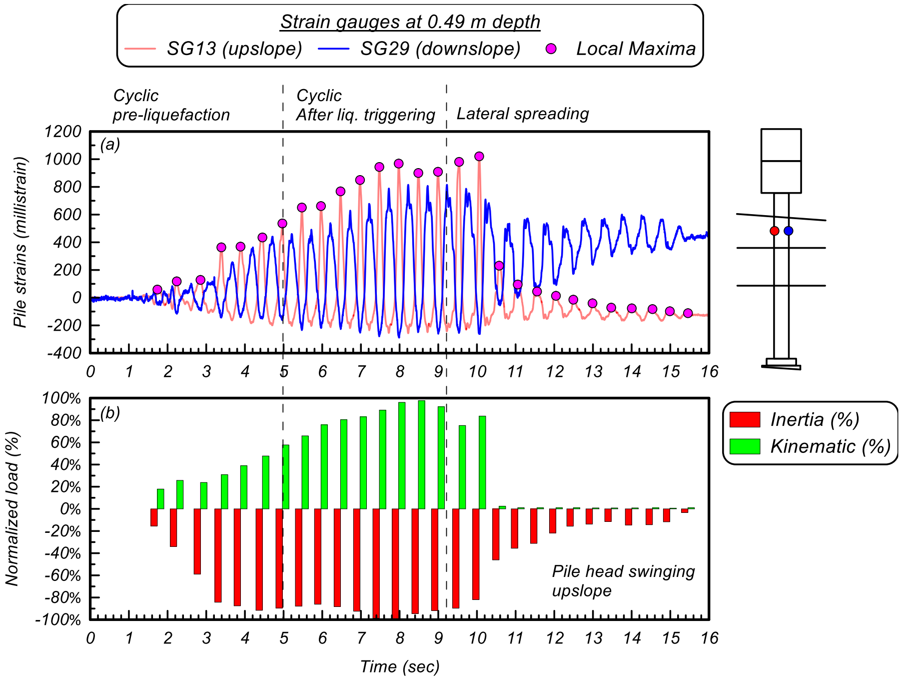

Figure 19. (a) Pile strains in two strain gauges at a depth of 0.49 m. (b) Normalized inertial and kinematic loads during peak pile strains at a depth of 0.49 when the pile head swings in the upslope direction.

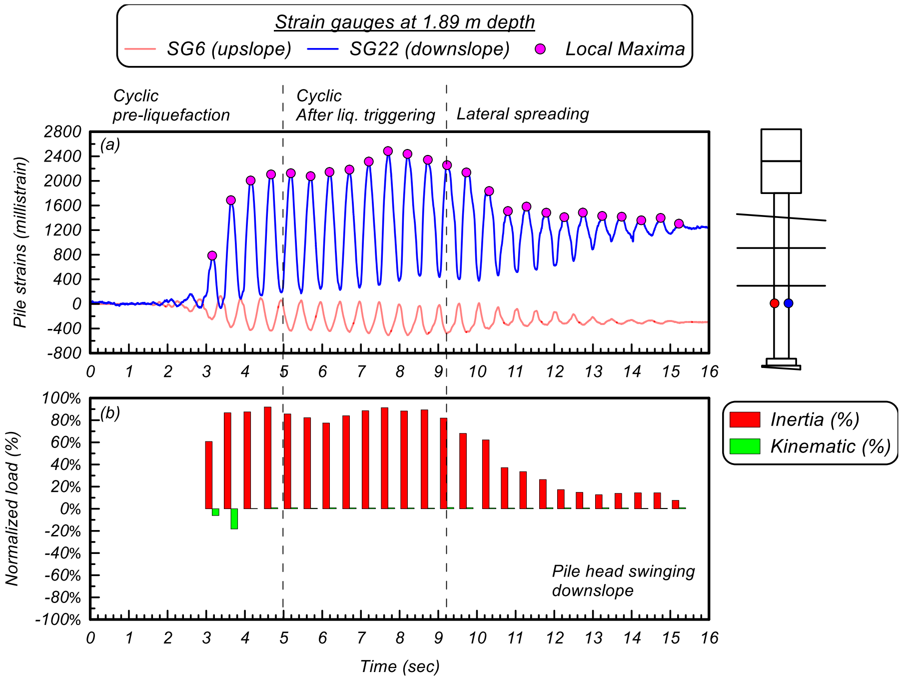

Figure 20. (a) Pile strains in two strain gauges at a depth of 1.89 m. (b) Normalized inertial and kinematic loads during peak pile strains at a depth of 1.89 m when the pile head swings in the downslope direction.

Table 7 summarizes the proportional values of I and K at selected cycles C and D when the pile strains are at, or close to, their peak values and porewater pressure ratios in the liquefiable sand layers.

Table 7: Proportional I, K, and R_u at select critical cycles corresponding to peak pile strains

Cycle	Time (sec)	I^a	K^a	R_u in Loose Sand	R_u in Dense Sand
C	7.70	+91%	+1%	0.73	0.45
D	7.98	− 100%	+98%	0.77	0.56

[a] Positive values indicate a downslope direction; negative values indicate an upslope direction.

3.3 Project Conclusions

The seismic behavior of a RC pile with a diameter of 0.25 m subjected to liquefaction-induced lateral spreading was investigated using a shake table experiment performed by Ebeido (2019). A sinusoidal motion was applied at the base of a model that was inclined by 4 degrees. The loose and dense sand layers liquefied during the test, resulting in a permanent lateral spreading displacement of approximately 0.4 m. The pile was subjected to the combined effects of inertial loads from the acceleration of the superstructure mass and kinematic loads from the overlying nonliquefiable, dry crust. The dynamic responses of the soil and pile were analyzed to evaluate the relative contributions of inertial and kinematic loads during critical cycles (i.e., at the time of maximum inertia and the time of maximum pile strains). The superstructure acceleration was considered to be representative of the inertia, and the normal soil pressures within the crust recorded using pressure transducer arrays attached to the upslope and downslope sides of the pile were considered to be representative of the kinematic crust load. The pile developed a plastic hinge at the base within approximately 9.25 sec, and excessive deformation and collapse followed shortly after. Considering that most piles are designed to be capacity protected (i.e., no plastic hinge is allowed to form in the pile), the combination of inertial and kinematic loads were examined in this study prior to pile failure.

It was found that large pile strains developed after liquefaction was triggered (after 5 sec). Large pile strains (and curvature) were recorded at a shallow depth within the crust (0.49 m) and a deeper location below the loose liquefiable sand (1.89 m). Large pile strains at shallow depth were found to be correlated with the inertial loads applied in the upslope direction. These upslope inertial loads were resisted by downslope crust loads, indicating an out-of-phase interaction. In contrast, large pile strains that occurred at deeper locations were correlated with downslope inertial loads and were accompanied by zero crust load, indicating that there was no lateral spreading force during the downslope inertial cycles. A gap at the downslope area in front of the pile formed because the soil displacements exceeded the pile displacements during the cyclic phase after liquefaction was triggered. The lack of crust load during the downslope inertial cycles is attributed to the pile head outrunning the crust displacement and causing the pile to be pushed into the gap at the downslope area in front of the pile.

The observations reported in this study are based on the results of a single shake table test and are limited to the soil and pile properties and the ground motion characteristics considered in this study. The interaction of inertia and kinematics appears to be a site- and project-specific phenomena. Therefore, the findings of this study—and, specifically, the lack of lateral spreading crust load during downslope inertial cycles—should be considered in design as one possible scenario in addition to the scenarios from several other studies that suggest combining the inertial loads with a lateral spreading force (e.g., Boulanger et al. 2007, Turner et al. 2016, Souri et al. 2022, Tokimatsu et al. 2005, Cubrinovski et al 2017) and the design guidelines listed in Table 1. The use of normal pressures as representative of kinematic loads in this study neglects the contribution of side shear from the nonliquefied crust in kinematic loads. While this contribution is expected to be smaller than the contribution of normal pressures, its inclusion may result in larger *K* values than those reported in this study to be combined with full inertial loads in the downslope direction. This contribution needs to be quantified in future studies.

4.0 CONCLUSIONS

Liquefaction triggering and its effects remain difficult to quantify. Section 2 finds the low plasticity alluvial silt subjected to a CDSS testing program provides results unique to the soil specimen that generally shares similar trends to similar regional soils. Importantly, the testing program finds that the soil tested has better cyclic performance than what would be estimated from simple correlations (e.g. those in Bray and Sancio 2006 or Idriss and Boulanger 2008). Test regimens like those described in section 2 will continue to contribute to local knowledge of liquefaction susceptibility and post-cyclic performance of low plasticity silts in the American Pacific Northwest. Section 3 explores the loading combinations exerted on a reinforced-concrete pile in a full scale shake table test. This test provides valuable data to calibrate geotechnical software models to lateral spreading effects, and provides methods for interpreting tests performed in this manner.

Overall, the research projects presented in this paper contribute to the body of knowledge to refine our understanding and characterization of liquefaction and its subsequent effects on soil and structures.

5.0 REFERENCES

American Association of State Highway and Transportation Officials (AASHTO). 2020. LRFD Bridge Design Specifications. 9th ed. Washington, D.C.: American Association of State Highway and Transportation Officials.

American Society of Civil Engineers (ASCE). 2014. Seismic Design of Piers and Wharves. ASCE/COPRI 61-14. Reston, VA: ASCE Standards Committee on Seismic Design of Piers and Wharves. https://doi.org/10.1061/9780784413487

ASTM. 2000. “Standard test methods for liquid limit, plastic limit, and plasticity index of soils.” ASTM D4318. West Conshohocken, PA: ASTM

ASTM. 2011. Standard Test Method for One-Dimensional Consolidation Properties of Soils. ASTM D2435-11. West Conshohocken, PA: ASTM.

ASTM. 2017b. Standard Test Methods for Particle-Size Distribution (Gradation) of Soils Using Sieve Analysis. ASTM D6913-17. West Conshohocken, PA: ASTM.

ASTM. 2019. Standard Test Method for Consolidated Undrained Cyclic Direct Simple Shear Test under Constant Volume with Load Control or Displacement Control. ASTM D8296-19. West Conshohocken, PA: ASTM.

ASTM. 2021. Standard Test Method for Particle-Size Distribution (Gradation) of Fine-Grained Soils Using the Sedimentation (Hydrometer) Analysis. ASTM D7928-21. West Conshohocken, PA: ASTM.

Ashford, S., Boulanger, R., and Brandenberg, S. 2011. “Recommended Design Practice for Pile Foundations in Laterally Spreading Ground.” Report PEER 2011/04, Pacific Earthquake Engineering Research Center (PEER), Berkeley, Calif. June.

Bray, Jonathan D., and R. B. Sancio. "Assessment of the liquefaction susceptibility of fine-grained soils." Journal of geotechnical and geoenvironmental engineering 132.9 (2006): 1165-1177.

Boulanger, Ross W., and I. M. Idriss. "Liquefaction susceptibility criteria for silts and clays." Journal of geotechnical and geoenvironmental engineering 132.11 (2006): 1413-1426.

Boulanger, R. W., Chang, D., Brandenberg, S. J., Armstrong, R. J., & Kutter, B. L. 2007. Seismic design of pile foundations for liquefaction effects. In: K.D. Pitilakis (ed.), Earthquake Geotechnical Engineering. Dordrecht: Springer. pp. 277–302).

California Department of Transportation (Caltrans). 2012. Guidelines for Foundation Loading and Deformation Due to Liquefaction Induced Lateral Spreading. California Department of Transportation, Sacramento, Calif.

Casagrande, Arthur. "The determination of pre-consolidation load and it's practical significance." Proc. Int. Conf. Soil Mech. Found. Eng. Cambridge, Mass., 1936. Vol. 3. 1936.

Cubrinovski, M., Bray, J. D., de la Torre, C., Olsen, M. J., Bradley, B. A., Chiaro, G., Stocks, E. and L. Wotherspoon. 2017. Liquefaction effects and associated damages observed at the Wellington CentrePort from the 2016 Kaikoura earthquake." Bull. N. Z. Soc. Earthq. Eng., 50(2): 152–173. https://doi.org/10.5459/bnzsee.50.2.152-173

Dahl, Karina R., et al. "Characterization of an alluvial silt and clay deposit for monotonic, cyclic, and post-cyclic behavior." Canadian Geotechnical Journal 51.4 (2014): 432-440.

DeJong, Jason T., et al. "Work-based framework for sample quality evaluation of low plasticity soils." Journal of Geotechnical and Geoenvironmental Engineering 144.10 (2018): 04018074.

Ebeido, A. 2019. Lateral-spreading effects on pile foundations: Large-scale testing and analysis. Dissertation. University of California, San Diego, Department of Structural Engineering, San Diego, Calif. https://escholarship.org/uc/item/3db527kh

Ebeido, A., & Elgamal, A. 2019a. Experimental Behavior of a Reinforced Concrete Pile During Liquefaction-Induced Lateral Spreading. In Geotechnical Engineering in the XXI Century: Lessons learned and future challenges. In: Proceedings of the XVI Pan-American Conference on Soil Mechanics and Geotechnical Engineering (XVI PCSMGE), 17–20 November 2019, Cancun, Mexico (pp. 453–460). IOS Press. https://doi.org/10.3233/STAL190071

Ebeido, A. & Elgamal, A., 2019b. Assessment of seismic behavior of deep foundations from large-scale liquefaction shake table experiments. In Earthquake Geotechnical Engineering for Protection and Development of Environment and Constructions (pp. 353-368). CRC Press.

Ebeido, A., Elgamal, A. and Zayed, M., 2019a, March. Large scale liquefaction-induced lateral spreading shake table testing at the University of California San Diego. In Geo-Congress 2019: Earthquake Engineering and Soil Dynamics (pp. 22-30). Reston, VA: American Society of Civil Engineers.

Ebeido, A., Elgamal, A., Tokimatsu, K., & Abe, A., 2019b. Pile and pile-group response to liquefaction-induced lateral spreading in four large-scale shake-table experiments. Journal of Geotechnical and Geoenvironmental Engineering, 145(10), 04019080.

Hamada, M., Yasuda, S., Isoyama, R., & Emoto, K. 1986. Study on liquefaction induced permanent ground displacements. Report for the Association for the Development of Earthquake Prediction, Chiyoda, Japan. November 1.

Idriss, I. M., & Boulanger, R. W. (2008). Soil liquefaction during earthquakes. Earthquake Engineering Research Institute.

Ishihara, K., & Yoshimine, M. (1992). Evaluation of settlements in sand deposits following liquefaction during earthquakes. Soils and foundations, 32(1), 173-188.

Jana, Amalesh, and A. W. Stuedlein. "Monotonic, Cyclic, and Postcyclic Responses of an Alluvial Plastic Silt Deposit." Journal of Geotech. and Geoenv. Engineering 147.3 (2021): 04020174.

Ladd, C. C., and R. Foott. "New design procedure for stability of soft clays." Journal of the geotechnical engineering division 100.7 (1974): 763-786. (SHANSEP)

Lunne, T., T. Berre, and S. Strandvik. 1997. “Sample disturbance effects in soft low plastic Norwegian clay.” In Proc., Int. Symp. On Recent Developments in Soil and Pavement, 81-103. Leiden, Netherlands: A.A. Balkmema

Martinez, J.A., Khosravifar, A., Ebeido, A., Elgamal, A.. (2022), Combined Effects of Liquefaction-Induced Lateral Spreading and Superstructure Inertial Loads on Pile Foundations. DFI Journal - The Journal of the Deep Foundations Institute, *16(2).*

Martinez, J., Khosravifar, A., Moug, D., & Sideras, S. Undrained Cyclic Shear Behavior of a Low Plasticity Alluvial Silt. In Geo-Congress 2023 (pp. 142-151).

Multidisciplinary Center for Earthquake Engineering Research/Applied Technology Council (MCEER/ATC). 2003. Recommended LRFD guidelines for the seismic design of highway bridges. Report No. MCEER-03-SP03. Multidisciplinary Center for Earthquake Engineering Research, University of Buffalo, Buffalo, N.Y. December 30.

Oregon Department of Transportation (ODOT). 2014. Geotechnical Design Manual. Oregon Department of Transportation, Technical Services Branch, Salem, Ore.

Port of Anchorage (POA) 2017. “Anchorage Port Modernization Project Seismic Design Manual.” Port of Anchorage, Anchorage, Alaska.

Port of Long Beach (POLB). 2015. “Port of Long Beach Wharf Design Criteria,” Version 4.0. Port of Long Beach, Long Beach, Calif. May.

Sanin, M. V., and D. Wijewickreme. 2011. “Cyclic shear response of undisturbed and reconstituted Fraser River Silt.” In Proc., Pan-Am CGS Geotechnical Conf. Richmond, BC, Canada: Canadian Geotechnical Society.

Simpson, D. C., & Evans, T. M. (2016). “Behavioral thresholds in mixtures of sand and kaolinite clay.” Journal of Geotechnical and Geoenvironmental Engineering, 142(2), 04015073.

Souri, M., Khosravifar, A., Dickenson, S., Schlechter, S., & McCullough, N. 2022. Pile-Supported Wharves Subjected to Inertial Loads and Lateral Ground Deformations. I: Experimental Results from Centrifuge Tests. Journal of Geotechnical and Geoenvironmental Engineering, 148(11), 04022090. https://doi.org/10.1061/(ASCE)GT.1943-5606.0002878

Terzaghi, K., R. Peck, and G. Mesri. 1996. Soil mechanics in engineering practice. New York: Wiley

Tokimatsu, K., Suzuki, H., & Sato, M. 2005. Effects of inertial and kinematic interaction on seismic behavior of pile with embedded foundation. Soil Dynamics and Earthquake Engineering, 25(7-10), 753–762. https://doi.org/10.1016/j.soildyn.2004.11.018

Turner, B. J., Brandenberg, S. J., & Stewart, J. P. 2016. Case study of parallel bridges affected by liquefaction and lateral spreading. Journal of Geotechnical and Geoenvironmental Engineering, 142(7), 05016001. https://doi.org/10.1061/(ASCE)GT.1943-5606.0001480

Vucetic, M., and R. Dobry. 1991. “Effect of soil plasticity on cyclic response.” J. Geotech. Eng. 117 (1): 89–107. https://doi.org/10.1061/(ASCE)0733-9410(1991)117:1(89).

Wang, L. B., and J. D. Frost. "Dissipated strain energy method for determining preconsolidation pressure." Canadian geotechnical journal 41.4 (2004): 760-768.

Washington Department of Transportation (WSDOT) 2021. Geotechnical Design Manual. M 46-03.14. Washington Department of Transportation, Olympia, Wash.

Wijewickreme, D., A. Soysa, and P. Verma. 2019. “Response of natural fine-grained soils for seismic design practice: A collection of research findings from British Columbia, Canada.” Soil Dyn. Earthquake Eng. 124 (Sep): 280–296. https://doi.org/10.1016/j.soildyn.2018.04.053

Youd, T. L., & Perkins, D. M. (1978). Mapping liquefaction-induced ground failure potential. Journal of the Geotechnical Engineering Division, 1